Myoglobin-derived iron causes phagocyte dysfunction, wound enlargement, and impaired regeneration in pressure injuries of muscle

N. Jannah M. Nasir[1,2], Hans Heemskerk[1,3], Julia Jenkins[1], N. Hidayah Hamadee[1], Ralph Bunte[1], Peter T. C. So[3,4], Lisa Tucker-Kellogg*[1,2,3]

Affiliations:

[1]Cancer & Stem Cell Biology, Duke-NUS Medical School, Singapore.

[2]Centre for Computational Biology, Duke-NUS Medical School, Singapore.

[3]BioSyM and CAMP Interdisciplinary Research Group, Singapore-MIT Alliance for Research and Technology, CREATE, Singapore.

[4]Departments of Mechanical Engineering & Bioengineering, Massachusetts Institute of Technology, Cambridge, MA, USA.

*Prof. Tucker-Kellogg, 8 College Road, Singapore 169857.

+65 8123 3490. Lisa.Tucker-kellogg@duke-nus.edu.sg

The authors have declared that no conflict of interest exists.

Keywords: chronic wound healing, ischemic muscle death, myogenesis, regenerative medicine, stem cells

Abstract

Pressure injuries are classified as chronic wounds, but the reasons for poor healing are not well understood, such as whether impairments are due to comorbidities and bacteria. Chronic vascular ulcers have pathologies caused by extracellular release of hemoglobin, so we questioned whether muscle pressure injuries (mPI) would have intrinsic pathologies due to extracellular myoglobin (Mb), and whether iron chelation therapy could improve them.

Healthy mice in specific-pathogen-free conditions received pressure injuries. Cohorts were Mb–/– versus Mb+/+ in elderly 20-month-olds, or adult Mb+/+ 5-month-olds treated with saline versus iron chelator (subcutaneous deferoxamine, DFO). For comparison, healthy control regeneration was created using cardiotoxin injection.

Unlike acute injuries, the wound bed of mPI displayed failure of phagocytosis at day 3, accompanied by high accumulation of iron, oxidative damage, and a lack of viable immune cells. The necrotic tissue was later expelled as slough (eschar). Mb-knockout mPI had undetectable levels of iron, low oxidative stress ($p<0.05$), greater immune infiltration (230%, $p<0.05$), 4-fold decreased marker for extracellular traps ($p<0.01$), and 50% smaller area of tissue death. Similar to knockout, injecting DFO after wounding caused improvement in oxidative stress (2-fold, $p<0.05$), extracellular trap marker (4-fold, $p<0.01$), and diameter of tissue killed (35%, $p<0.05$). In other words, tissue margins could be protected from dying. At later timepoints, DFO-treated wounds had higher levels of viable immune infiltrate ($p<0.05$), greater extent of muscle regeneration (46% smaller diameter of gap, $p<0.01$), and superior myofiber morphology ($p<0.0001$).

We conclude that myoglobin iron from mPI causes oxidative stress and delayed infiltration, despite a lack of infection. Remarkably, tissue viability could be salvaged by post-injury treatment with subcutaneous injections of an FDA-approved iron chelator. This work also sheds light on how a hostile wound microenvironment impairs myogenesis and morphogenesis.

Introduction

Pressure injuries (also called pressure ulcers, bedsores, decubitus ulcers, or pressure sores) are tissue damage caused by sustained pressure. They are extremely painful (1), costly to prevent and treat (2), and they increase the risk of patient sepsis and death (3). Tissue death can be caused by mechanical deformation, ischemia, or both. Ischemia is often studied as ischemia-reperfusion injury, but poor clearance of waste and damage factors (4) may be equally important.

Pressure injuries often heal more slowly than other seemingly-comparable injuries (5), especially if they involve deeper layers such as muscle (6, 7). Pressure injuries are classified as chronic wounds, but the reasons for slow healing are unclear. Some cases of slow healing can be explained by complications, infection, or co-morbidities, but diabetes and vascular disease are not required, and pressure injuries can affect any immobile person (e.g., spinal cord injury). Healing can be delayed by noncompliance with off-loading (i.e., if a patient rests weight on the injured region), but some patients may be incorrectly suspected of noncompliance when the wound is dysfunctional for other reasons. In this study, we ask whether some aspect of pressure-induced injuries might be intrinsically inhospitable to regeneration and amenable to intervention.

Chronic ulcers of veins or arteries, particularly venous stasis ulcers and sickle cell ulcers, have high levels of extracellular hemoglobin (Hb) released in the wound. For example, many have deposits of hemosiderin. Extracellular Hb and its breakdown products (e.g., hemin, iron) create oxidative stress (8, 9) and other effects that are detrimental to regeneration. For example, Hb decreases nitric oxide for angiogenesis (10, 11), and signals as a DAMP (damage-associated molecular pattern) to increase inflammation (12, 13). Intriguingly, Hb is an innate immune factor with evolutionarily-conserved antimicrobial function in the extracellular environment. When activated by proteolytic cleavage, bacterial binding, and/or conformational change, Hb or its cleavage fragments are weaponized to produce higher levels of ROS (reactive oxygen species). This process has been called “oxidative burst without phagocytes” (14, 15). Our earlier work used evolutionary conservation to identify Hb peptide sequences for producing high ROS, and Hb interaction with coagulation via tissue factor (16, 17). Therefore, an innate immune program has been conserved by evolution to hold extracellular Hb in place and to amplify its toxicity, in addition to the better-known system that detoxifies hemoglobin and sequesters iron away from invading pathogens (18).

Myoglobin release into plasma or urine has been observed after muscle pressure injuries (mPI) in multiple studies including DTI (deep tissue injury) (19-21), but was studied as a readout of damage rather than as a source of regenerative dysfunction. We reason by analogy to hemoglobin that extracellular myoglobin might create a hostile wound environment. An extracellular environment oxidizes globins to a ferric (Fe^{3+}) state, which can be further oxidized to ferryl ($Fe^{IV} = O$) globin in the presence of endogenous peroxides such as hydrogen peroxide (22). Hydrogen peroxide is ubiquitous in contexts of cell stress, mitochondrial permeabilization, and cell death (23). Ferryl-Mb can oxidize macromolecules directly (8, 24, 25) and can form heme-to-protein cross-links (26). Most importantly, ferryl myoglobin can participate in a catalytic cycle of pseudo-peroxidase activity (redox cycling) (27). In a tissue context, myoglobin can induce ferroptosis, which is a form of non-apoptotic cell death associated with iron and characterized by lipid peroxidation (28). Dissociation of myoglobin into free heme or iron results in additional forms of toxicity, as described for hemoglobin.

We hypothesize that mPI will have Mb-dependent dysfunctions that resemble the Hb-dependent dysfunctions of vascular ulcers, and that this toxicity will differ from other forms of muscle death (modelled in the laboratory using an injection of cardiotoxin). Furthermore, we hypothesize that either Mb-knockout or iron chelation therapy will partially normalize the process of injury response in mPI.

Deferoxamine (DFO), also known as desferrioxamine or desferoxamine, is an FDA-approved small-molecule iron chelator that improves iron overload syndromes (29, 30). DFO binds free iron and heme at a 1-to-1 ratio (29), scavenges free radicals (22, 31), reduces ferryl myoglobin to ferric myoglobin (25, 32), inhibits cross-linking of heme to protein (9), and prevents the formation of pro-oxidant globin and heme species. In our study, subcutaneous DFO is used for combatting local iron overload and/or mimicking myoglobin knockout. Prior studies have used DFO for another role in wound healing: DFO can induce hypoxia-response genes such as VEGF because an iron-dependent enzyme regulates the degradation of Hif1α (33). Due to its activation of hypoxic signaling, DFO has long been used in bioengineering for promoting angiogenesis (34, 35).

Assessing the contribution of myoglobin iron to pressure injury pathophysiology provides an opportunity to test several additional hypotheses about pressure injuries. First, the poor healing of pressure injuries is often attributed to co-morbidities and complications. To the best of our knowledge, pressure injuries have never been assessed for poor regeneration under aseptic conditions in young, healthy animals. We hypothesize that even under these ideal circumstances, mPI will heal slowly and incompletely. Second, our prior work in mathematical modeling predicted that oxidative stress from myoglobin and other DAMPs could expand a region of tissue death after pressure is removed, as a mechanism of secondary progression (36). Secondary progression has been observed in pressure injuries (37), but blocking secondary progression has not been clinically recognized (38) as one of the goals of treatment. Therefore, our measurements will test whether the tissue margins can be saved from dying by Mb knockout and/or iron chelation therapy. Third, prior studies found that high levels of heme/hemin caused impairment of phagocyte functions of chemotaxis and phagocytosis (11, 39-43). Given that pressure ulcers often have slough or eschar, we hypothesize that phagocytosis will also be impaired in mPI, and that sterile mPI will have slough, despite the absence of bacterial biofilm. If correct, this would imply that slough is not sufficient by itself to conclude there is infection in a wound. Fourth, we hypothesize that iron chelation therapy, by improving the early stages of injury response, will lead to better morphogenesis and tissue architecture in long-term regeneration, even after treatment has ended. This hypothesis will be tested by breeding inducible fluorescence into satellite cells, so that newly regenerated muscle fibers will be labelled against the background of pre-existing muscle.

Results

Magnet-induced pressure injury causes delayed healing and failure of muscle regeneration

To compare wound healing between acute and chronic wounds, we injured the dorsal skinfold of mice using either cardiotoxin (CTX) or pressure (Suppl. Fig 1A-B) in healthy young adult mice under specific pathogen-free conditions. The normal uninjured mouse skinfold contains the following parallel layers: a thin epithelium (epidermis), a thicker layer of dermis, dermal white adipose tissue (dWAT), a muscle layer called the panniculus carnosus (PC), and a wavy layer of loose areolar tissue (Suppl. Fig 1C). After CTX

killed the panniculus muscle, substantial muscle regeneration occurred by 10 days, in which immature muscle fibers displayed central nuclei (Fig 1A). At 40 days after acute injury, muscle was completely regenerated and mature, with peripherally-located nuclei (Fig 1C). In contrast, the pressure-injured wound bed remained filled with dead tissue at day 10, indicated a failure of phagocytosis to clear the necrotic tissue (Fig 1B, 1E-F). Our pressure injuries showed no signs of infection and no epibole (Fig 1E). The dead epidermis, dermis, dWAT and panniculus layers were pushed upward at day 5 ± 2 as slough (necroslough, per the nomenclature of (44)) and remained at the surface, becoming a dry eschar (Fig 1E). When the eschar dropped off (by day 15), the size of the epithelial opening was smaller than the eschar, meaning that re-epithelialization had occurred underneath the eschar. Re-epithelialization completed at day 21 ± 2. Despite successful closure of the epithelial layer, pressure injuries at 40 days had only partial regeneration of the panniculus carnosus layer (Fig 1D, 1G). At 90 days after pressure injury, the dermis and epidermis had regenerated, but a hole remained in the panniculus muscle layer (Fig 1H), indicating a failure to regenerate (45). Suppl. Fig 2 provides a Gantt chart schematic to summarize the difference in timing and milestones, between the healthy healing of CTX damage, versus the impaired healing of pressure-induced damage. We conclude that mPI heal poorly in the absence of miocrobial pathogens and co-morbidities.

Compressed regions of pressure injury display failure of immune infiltration

To understand the failure of phagocytosis at day 10, we studied tissue sections from day three post-injury. Both cardiotoxin-induced and pressure-induced injuries had comprehensive death of muscle tissue, as indicated by karyolysis (dissolution of nuclear components), karyorrhexis (fragmentation of the nucleus) and acidification (eosinification) in H&E staining of the panniculus carnosus (Fig 2B). Cardiotoxin and pressure injuries had a difference in morphology: cells in pressure-injured tissues were flattened, and the thickness of the panniculus muscle layer was half of uninjured (Fig 2A-C; $p < 0.0001$). Even more striking was the difference in immune cell numbers. The muscle layer of cardiotoxin wounds had 325% higher levels of immune cell infiltrate than mPI ($p < 0.0001$; Fig 2A-B, and Fig 2D). The panniculus layer of mPI was nearly devoid of intact immune cells. The absence of immune cell infiltrate is noteworthy because macrophages have specialized functions for iron-scavenging (46, 47), and because free iron, when not adequately scavenged, can over-stimulate the innate immune response (48).

Another difference between mPI and CTX was in the level of citrullinated histone-3 (citH3), a marker of extracellular traps (ETs). ETs are formed when phagocytes citrullinate their histones and eject nuclear and/or mitochondrial DNA (and associated factors), which can trap and kill pathogens during infection. The cell often dies in the process (ETosis). Extracellular traps (ETs) have been observed in sickle cell ulcers (49). In day 3 wounds, levels of citrullinated histone-3 (citH3) were 6-fold higher in mPI than in CTX (Fig 2E-G; $p < 0.01$). Highest levels occurred near the muscle layer, such as the interface between the panniculus layer and the dWAT or dermis. This is consistent with the possibility that immune cells may have been present in the muscle layer of mPI before day 3 and then died of ETosis. Oxidative stress is a well-studied trigger of ETs, and other stimuli include hemin and heme-activated platelets (50, 51).

Free iron remains in wound tissues after pressure injury

Free iron, measured by Perls' Prussian blue stain, was very high in mPI (Fig 2I), but undetectable at the same time-point after cardiotoxin injury (Fig 2H-J). Prussian blue selectively detects ferric Fe^{3+} in tissue, such as ferritin and hemosiderin. The blue speckles in Fig 2I are iron deposits in the extracellular matrix, and the blue ovals are iron-loaded immune cells (46, 47). Heme oxygenase-1 (HO-1) is an enzyme

that performs heme degradation and other functions, and it serves as a marker of high heme or iron. HO-1 was also increased in mPI sections by 40% (Fig 2K-M; $p < 0.001$) compared with cardiotoxin injury. HO-1 expression was localized to the panniculus layer after CTX, but it was widespread across all layers after mPI.

Extracellular myoglobin harms macrophage viability *in vitro*

Because immune cells were absent from the wound bed of mPI at Day 3, we asked whether free myoglobin (Mb) is cytotoxic to monocytic cells. Incubation of RAW264.7 cells in media containing 50 µg/ml myoglobin (comparable to levels in muscle lysate) caused cell death and decreased ATP production by 46% ($p < 0.0001$), compared to cells cultured in media alone or treated with canonical M1 or M2 stimuli (Suppl. Fig 3A-B). *In vitro* studies of oxidative stress can have extensive artifacts (52, 53), so we returned to the tissue context for studying Mb knockout.

Myoglobin knockout mPI have less death and a less abnormal immune response

We developed Myoglobin knockout (Mb−/−) mice via CRISPR deletion of the entire gene in the germline. Note that prior studies of adult Mb−/− mice found no obvious phenotype (54-56). Mb−/− is often lethal to cardiac development during E9.5-E10.5, but some Mb−/− embryos survive to term (56). Among our Mb−/− that were born, all developed with normal feeding, weight gain, grooming, social behaviour, and lifespan. Deletion of Mb was confirmed by Western blotting (Suppl. Fig 4A), immuno-staining (Suppl. Fig 4B-C), and DNA gel electrophoresis (data not shown). With H&E staining, we detected no knockout-induced changes to the tissues of our injury model (skin, dWAT, panniculus carnosus layer, or loose areolar tissue) other than increased capillary density (by 17%, $p < 0.05$; Suppl. Fig 4D) and increased thickness of the dWAT layer in Mb−/− mice (by 43%, $p < 0.05$, Suppl. Fig 4D). Total iron was not significantly decreased ($p = 0.066$, Suppl. Fig 4E).

We compared pressure ulcers in Mb−/− versus Mb+/+ mice (Suppl. Fig 4F) using elderly 20-month-old animals. (The mPI in elderly were similar to mPI in young, except with milder increases in pressure-induced oxidative damage, Suppl. Fig 5). At day 3 post-injury, Mb-wildtype mice had high levels of iron (Fig 3A), which appeared in the muscle, dWAT, and dermis, including both the extracellular space and in the small numbers of infiltrating immune cells. In contrast, Mb knockout mice had no detectable signal from Perls' stain in any layer of the wound (Fig 3B-C). HO-1 was also decreased two-fold in Mb−/− mPI compared to Mb+/+ (Fig 3D-F). Levels of immune cell infiltrate were 2.3-fold greater in Mb-knockout compared to Mb+/+ (Fig 3G-I; $p < 0.05$). In summary, measures of innate immune response became less abnormal after Mb-knockout.

The wound size was smaller in Mb-knockout than Mb-wildtype ($p < 0.05$, measured as external area, Fig 3J and Suppl. Table 1). Histopathology scoring in the centre of the wound showed 50% decreased tissue death ($p < 0.01$, Fig 3G-H and Fig 3K). Oxidative damage was markedly decreased in Mb-knockout according to all of the following measures: DNA damage (8-OG, 8-hydroxy-2'-deoxyguanosine) was > 5-fold lower (Fig 4A-E; $p < 0.01$); lipid peroxidation (measured using BODIPY 581/591) was 1.3-fold decreased (Fig 4F-J; $p < 0.05$); and protein damage (measured using 3-nitrotyrosine, NTYR) was 1.5-fold decreased (Suppl. Fig 6A-E; $p < 0.01$). Mb−/− wounds showed roughly four-fold decrease in CitH3 (Fig 4K-Q; $p < 0.01$). These improvements in the wound microenvironment affected more than just the muscle layer, because Mb-wildtype wounds had high levels of CitH3 throughout the wound, and high levels of BODIPY and NTYR in the dWAT and dermis as well as muscle.

A panel of cytokines, chemokines and growth factors were measured in muscle homogenate of mPI from +/+ versus −/− at day 3 (Suppl. Table 2). Correction for multiple hypothesis-testing was performed using two-way ANOVA, and there was no change in total protein levels between the homogenate of +/+ and −/−. The Mb−/− wounds had lower levels of CXCL16, a cytokine associated with lipid peroxidation (57) (Suppl. Table 2; $p < 0.05$) and higher levels of PAI-1 (Serpin E1), a protease inhibitor associated with TGFβ (Suppl. Table 2; $p < 0.01$).

Effects of iron chelation therapy on secondary progression of the wound

Given the strong benefit of Mb knockout, we sought another orthogonal intervention to confirm the role of myoglobin iron. We administered an FDA-approved iron chelation drug deferoxamine (DFO) via injection under the dorsal skinfold of 5-month-old mice. The mice received DFO or saline control for up 16 days (Fig 5A), and tissue was analysed at 3, 7, 10, 40, and 90 days (Suppl. Table 3).

Remarkably, DFO treatment caused a decrease in the amount of muscle tissue that died from the initial pressure injury, even though the treatment didn't begin until 12 hours after the magnets were removed. At day 3 of treatment, DFO-treated wounds had 35% smaller diameter of dead PC tissue in cross-sections (Fig 5B; $p < 0.01$). This is consistent with our computational modeling prediction (36) that myoglobin-induced oxidative stress might alter the tipping point between survival and death, for a significant area of potentially viable tissue at the margins of the injury.

Effects of iron chelation therapy on injury response at day 3

Consistent with decreased tissue death, DFO-treated mPI displayed 7-fold lower levels of iron deposition by Perls' Prussian blue, compared with saline control at day 3 (Fig 5C-E). As in the elderly mPI, the young saline-treated mPI had iron accumulations in the extracellular space and immune cells of multiple layers, not just muscle (Fig 5C). HO-1 was similarly affected (Fig 5E-G; $p < 0.05$). To confirm that wounds were properly induced, Fig 5I-L show complete tissue death at the centres of the wounds in all animals, and skin was unaffected (Fig 5M).

DFO-treated wounds displayed less oxidative damage, as indicated by a 1.2-fold decrease in 8-OG (Fig 6A-E; $p < 0.05$), and two-fold decrease in BODIPY 581/591 (Fig 6F-J; $p < 0.001$). Change in protein nitration was not significant (Suppl. Fig 7A-E). Citrullinated histone-3 (CitH3) dropped to undetectable levels in DFO-treated sections (Fig 6K-Q; $p < 0.01$). The high CitH3 found in control wounds was partially co-localized with F4/80, a pan-macrophage marker (Suppl. Fig 8A-C), but some of the CitH3 may have been generated by earlier cells, no longer present. Suppl. Table 4 shows levels of various cytokines, chemokines and growth factors measured in DFO- versus saline-treated mPI at day 3 after injury. CXCL16 levels decreased by 36% ($p < 0.05$; Suppl. Table 4).

Effects of iron chelation therapy on immune infiltration and regeneration

At 7 days, DFO-treated tissues displayed 1.7-fold greater immune infiltration (Fig 7L; $p < 0.05$), including more than two-fold higher iNOS (Fig 7A-D and Fig 7K; $p < 0.05$), which is a marker of inflammatory stimulation in many cell types. At day 10, DFO-treated wounds still had higher levels of immune infiltrate ($p < 0.001$ for histopathology and $p < 0.01$ for count of DAPI nuclei), many of which were positive for Arginase-1 (Fig 7E-J and Fig 7M-O). Arginase-1 contributes to polyamine synthesis in wound healing. At day 10 of DFO-treatment, levels of Arginase-1 were two-fold higher in the wound bed (Fig 7N; $p < 0.01$) and immune cells showed almost three-fold greater distance of infiltration into injured tissue

(Fig 7P; $p < 0.05$) compared to saline-treated control. Granulation was also dramatically improved. Granulation is a crucial stage of regeneration characterized by proliferation of epithelial, endothelial, and fibroblast cells, and the formation of new capillaries (with continued presence of immune infiltrate). In DFO-treated pressure ulcers, the number of small blood vessels was twice as high as in saline-treated (Suppl. Fig 9A-G; $p < 0.05$). DFO-treated tissues also had roughly 315% higher expression of VEGF (Suppl. Fig 9H; $p < 0.05$).

Epithelial and muscle layers were differently affected. The epithelial layer closed at day 20 to 23 (Suppl. Fig 10A-F). Meanwhile, despite complete regeneration of the epidermis and dermis, the saline-treated panniculus carnosus failed to fully regenerate after pressure injury (Fig 1H). A hole remained in the panniculus layer at 40 days (in 7 out of 7 mice) and 90 days (in 5 out of 5 mice). For example, in Figure 1D, note that the adipose layer is immediately adjacent to loose areolar tissue at the wound centre, indicating that the panniculus layer is absent.

Quality and quantity of regeneration

DFO treatment improved the extent of muscle regeneration (Fig 8A-F). Much of this improvement was complete by day 40, when treatment yielded 546% more regeneration at the wound centre (Fig 8E; $p < 0.05$) and 65% more regeneration at the wound edge (Fig 8F and Suppl. Fig 11A-B; $p < 0.05$). In saline-treated wounds, myoblastic cells were observed at 40 days (Fig 8A and Fig 8C), indicating that muscle regeneration was still underway. When we extended the study to 90 days, no further increase in panniculus regeneration was detected (from 40 to 90 days) in saline-treated mPI. At the day 90 endpoint, DFO-treated wounds had significantly smaller gaps in the original region of muscle (46% smaller area of un-regenerated muscle; Fig 8G; $p < 0.01$) compared to saline.

Compared to healthy regeneration (Fig 9A-C, cardiotoxin-injured), the newly regenerated myofibers in saline-treated wounds had pathological morphology, seen from branched or split fibers, thin fibers, wavy instead of straight axes, and disjoint angles between different bundles of fibers (Fig 9D-F). Newly regenerated myofibers were distinguishable from pre-existing or never injured myofibers by their expression of fluorescent proteins, because our mice expressed the confetti transgene in Pax7-positive satellite cells and their progeny (45, 58). DFO-treated tissues displayed a far lower frequency ($p < 0.0001$) of morphological malformations than saline-treated tissues (Fig 9G-J).

Discussion

We used a standard magnet-induced model of pressure ulcers in mice, and instead of focusing on the skin healing, which is rapid and successful in rodents, we focused on the thin muscle layer beneath – the panniculus carnosus, also called the cutaneous muscle or the panniculus layer. This muscle regenerated slowly and incompletely from the magnet injury, providing a novel non-infected, non-diabetic (normoglycemic) animal model of impaired healing. The reason for poor healing was hypothesized to be accumulation of myglobin iron, based on inspiration from poor-healing wounds with hemolysis (e.g., sickle cell) and hemosiderin (e.g., venous insufficiency), and based on reports that mPI causes myoglobinuria (19, 59, 60).

To determine the role of myoglobin iron, we knocked out myoglobin unconditionally from the germline. As expected, the iron deposits seen after mPI injury were absent from knockouts. Similarly,

knockouts had far less oxidative and nitroxidative damage. One possible reason for oxidative and nitroxidative damage is because oxidized globins have peroxidase-like catalytic activity, and can catalyse nitrite oxidation and tyrosine nitration during ischemia (61). The peroxidase-like catalytic activity of myoglobin is particularly relevant in wounds, where endogenous H_2O_2 is provided by stressed, ischemic, or dying cells (62). Because myoglobin normally serves to supply oxygen in muscle tissue, one might expect Mb−/− mice to experience increased tissue death due to ischemia, but prior work showed Mb−/− mice are "surprisingly well adapted" to hypoxic conditions (63), capable of withstanding adrenergic stimulation (56), exercise and oxygen flux (55). Taking this one step farther, we found that possessing wildtype Mb caused 50% greater extent of tissue death during ischemic compression. We conclude that a large fraction of tissue death in the mPI was downstream of Mb. Multiple DAMPs and heme proteins probably contributed, but removal of Mb was sufficient to alleviate the overload.

The large effect-size seen with Mb-knockout (or iron chelation) raises the question of why myoglobin iron would be so disruptive. Nonspecific iron damage is an obvious explanation, but specific vulnerabilities may also be involved. Bacteria have evolved elaborate strategies to seize iron from hosts (e.g., the siderophore enterobactin, which has Ka = 10^{52} (64)). Thus, mammalian hosts have the hepcidin/ferroportin program to sequester iron inside intestines or macrophages during inflammation. Nevertheless, some pathogens (e.g., hemolytic streptococci) can liberate iron faster than the host can sequester it. This life-threatening scenario is the typical explanation given for why the innate immune system would have evolved mechanisms to amplify the oxidative damage of respiratory proteins (e.g., triggered by binding bacterial LPS), rather than simply detoxifying them (14-17). Another possible scenario is that pathogens evolved a capacity to liberate the iron from macrophages by exploiting phagocytosis; in response, mammalian hosts could have evolved a compensatory strategy to withhold phagocytosis in favor of ETosis during high-iron inflammation. A scenario of that sort would help explain the contrast we observed between high levels of pro-inflammatory biochemistry, but lack of phagocytosis. At later time points when immune cells were present in the wound bed, the dead tissue still was not phagocytosed. Many disorders of sterile inflammation display pathological persistence of nonviable matter (e.g., atherosclerotic or neurodegenerative plaque) but the study of wound healing offers the unique advantage of having a well-defined endogenous measure of phagocytic function in a physiological context.

To confirm the causal role of myoglobin iron, we injected DFO into mPI of 5-month-old mice. DFO treatment decreased levels of iron (Prussian blue) and oxidative stress (BODIPY and 8-OG), and other markers of a harsh environment (HO-1, CitH3, and CXCL16). Evidence in support of ferroptosis included high iron, lipid peroxidation, oxidative stress, and CXCL16. Damage in H&E sections was indicated by karyolysis and karyorrhexis.

Although we expected Mb−/− would lessen muscle death from mPI (36), we were surprised that the entire wound size improved, not just the muscle. The most reactive species of iron toxicity (i.e., hydroxyl radical) act locally at the site of creation, but milder ROS species and globin proteins can travel. Future work should repeat Mb depletion in inducible knockouts to address the possibility of developmental compensation, which could affect tissue resiliency.

We were also surprised that DFO-treated mPI had significantly smaller diameters of muscle death than saline-treated, because it was unclear whether a 12 hour delay in treatment would be soon enough to rescue the cell fate. (Note that 35% smaller diameter yields 58% smaller area for a circle.) From the combined evidence of knockout and drug, we conclude that myoglobin iron did cause secondary

progression in mPI. Furthermore, a non-trivial amount of secondary progression occured between 12hr and 72hr in the muscle, and was prevented by anti-iron drug treatment. In other words, muscle tissue continued to die after pressure was removed, and the extent of death was worsened by myoglobin iron, directly or indirectly. Secondary progression of wounds is well-documented in thermal burns, where partial-thickness tissue death can progress to full-thickness during the period after injury. There are multiple iron-related phenomena in pressure injuries that could contribute to secondary progression in this time period. Ferroptosis (65, 66) is likely, but we cannot rule out reperfusion injury, platelet activation, and DAMP-induced apoptosis / necroptosis (36). In summary, we found that iron chelation therapy could rescue tissue viability, even though it was not applied until the morning after pressure was removed.

The failure of phagocytosis and the persistence of necrotic debris in mPI was particularly striking when compared against cardiotoxin-induced muscle death. Immune cells were essentially absent from the pressure-injured muscles of young mice at day 3. The wounds exhibited a normal spike in immune cell infiltration outside the wound margins, moving toward the wound (Suppl. Fig 6B), but infiltrate was not seen inside the compressed region, almost as if infiltration had been halted at the boundary. Initially we questioned whether the altered architecture of the tissue might have blocked cell migration or occluded natural channels of migration. Closer inspection revealed that dead immune cell fragments and inflammatory markers such as CitH3 were present in the compressed region (Suppl. Fig 6A), suggesting that immune cells had been present before dying (infiltrated and/or tissue-resident). Our interpretation of the CitH3 and oxidative stress is that the high-iron wounds displayed an unexpected combination of both excessive and inadequate immune response – excessive in terms ROS and CitH3 markers, but inadequate in phagocytic activity. Other syndromes with iron overload have been recognized for decades to have poor function of phagocytes (67-69). For example, in patients with thalassemia major, neutrophils and macrophages exhibit poor chemotaxis, defective lysis, and impaired phagocytosis (41, 70). Similar phenomena occur in hemolysis (43) and endometriosis (42). In our mPI, immune infiltration was improved by knockout of globin-protein or iron chelation therapy. Mb-knockout wounds showed a 3.5-fold increase in immune cell infiltration compared to wildtype at day 3, and DFO-treated wounds showed improved infiltration at day 7 and day 10. These increases were especially prominent in the loose areolar tissue, but consistent across muscle, fat, and skin.

CitH3 levels were high in both conditions that had high iron deposits (young and elderly mPI) and low in the three conditions that lacked iron deposits (cardiotoxin, knockout, DFO-treated). This is consistent with prior work showing that various phagocytic cell types produce ETs upon exposure to heme (51), oxidative stress, or heme-activated platelets (50). ETs can help combat microbial pathogens but are detrimental to regeneration, and ETs contribute to many disorders of sterile inflammation. Our induction of CitH3 was likely sterile as well: the mouse environment was negative for 39 categories of pathogen (Suppl. Table 5, including common dermal microbiota *P.aeruginosa* and *S.aureus*), and no bacteria could be detected in or near the wound by Gram staining.

Slough is one of the clinical features of chronic and non-healing wounds (71), and it is often interpreted as sign of infection/inflammation. This information affects how wounds are treated, but in our study, slough was formed in the absence of any detectable microbial pathogens, and it reflected insufficient phagocytic activity. It is conventional wisdom that chronic wounds suffer from too many immune cells, but the mPI injury-response differed from that expectation. The biochemical environment of day 3 mPI included characteristics of a strong inflammatory response (ROS, CitH3) but without the

expected numbers of immune cells. Therefore, the mPI exhibited a mismatch between the strength of the biochemical program versus the cellular program of innate immune response.

In the sloughing process, dead skin layers and panniculus muscle were pushed to the surface while granulation expanded below. The viable tissue must have exerted upward mechanical force on the dead tissue, as indicated by the morphological distortion of the previously parallel geometry in the healthy margins. The slough remained at the surface but attached to the wound for roughly another 10 days before it detached spontaneously. There is much clinical debate about whether slough should be debrided. Removal depends on whether it plays a cytotoxic or protective role. Slough is an umbrella term describing multiple types of nonviable matter extruded from a wound bed. Slough is categorized as necroslough (of dead tissue), leukoslough (of inflammatory infiltrate), bioslough (of biofilms) and fibroslough (of extracellular matrix and fibroblasts) (44, 72). In our studies, eschar arose from necroslough, and re-epithelialization proceeded beneath it, so we conclude it was not cytotoxic, and was likely protective. This is consistent with clinical guidelines that debridement is contraindicated for an intact eschar, provided there is no evidence of infection (73). Human pressure injuries of category 3+ often have eschar (74), which makes many wounds unstageable (74, 75). Interestingly, the eschar that offered protection during the second week was evolved from a necrotic mass that was likely toxic at the start. Toxicity is inferred from the oxidative damage at day 3, and indirectly inferred from the phenomenon of secondary progression.

DFO treatment caused increased granulation tissue at 10 days, accompanied by higher expression of pro-angiogenic markers VEGF and endoglin. The angiogenic benefits of DFO have been widely reported in previous studies, where the mechanism of action was presumed to be stabilization of Hif1α (34, 35). HIF1α is degraded under normoxic conditions, whereas under hypoxia, the iron- and O_2-dependent hydroxylation and degradation of Hif1α is decreased (76). Thus, iron chelators such as DFO can block HIF1α degradation, resulting in transcription of hypoxia-tolerance and angiogenic factors. However, a less recognized regulator of angiogenesis is myoglobin. Prior studies found that over-expression of myoglobin not only failed to protect against ischemic death of muscle tissue, but indeed impaired the subsequent angiogenesis (77, 78). This is consistent with our finding that knocking out Mb improved tolerance to ischemic death of muscle tissue. In summary, DFO had strong pro-angiogenic benefits, but we cannot discriminate which fraction of the effect might be independent of Hif1α.

The impact of iron on macrophage polarization has frequently been reported, with M2 polarization downregulated (79) or upregulated (80) depending on dose or context. Iron-scavenging macrophages from an iron-loaded tissue displayed both inflammatory (iNOS, IFNγ) and alternately-activated (Arg1, IL10) markers (81), which is consistent with our finding that both iNOS and Arg1 levels increased with iron chelation.

Although DFO has been reported to cause negative side-effects in healthy muscle, we found no detrimental effects on the iron-loaded wound bed of dead muscle. Instead, DFO treatment improved the extent of muscle regeneration, both short-term (day 10) and long-term (day 90). DFO-treated tissues had smaller holes in the muscle sheet (i.e., smaller diameters for the region not regenerated at day 90) compared to saline-treated tissues. The morphology of the regenerated myofibers also improved, because the saline-treated muscles displayed frequent myofiber defects such as branching and non-parallel alignment. Split fibers are considered defective regeneration (82) and are especially vulnerable to re-injury (83).

Skin regeneration was not significantly affected by subcutaneous DFO. Previous work found DFO accelerated skin closure (34), but they used diabetic wounds with topical drug delivery. Other work studied the antioxidant and angiogenic benefits of DFO in preclinical models of ischemia-reperfusion injury (84-86), and we observe similar effects in mPI. Furthermore, we tracked the pro-regenerative benefits of DFO to the 90-day endpoint of improved tissue architecture and normalized myofiber morphology.

Previous studies using the same magnet injury model have focused their analysis on the skin (37, 87), but one study did note that the panniculus layer was absent at day 10 and reappeared at day 20 (87). Muscle-oriented studies have chosen larger muscle groups such as the hindlimb (tibialis or gluteus muscle) (88-90), trochanter (91, 92) or panniculus together with latissimus dorsi muscle (93). The panniculus carnosus muscle is highly relevant to human pressure injuries because humans have a panniculus layer at the heel (45, 94), and the heel is one of the most common locations for high-stage pressure injuries to occur. Impaired regeneration of the panniculus layer deprives soft tissues of cushioning (45, 95) which could promote wound recurrence.

Muscle damage can be achieved with cardiotoxin, a snake venom that causes myolysis (cytolysis) of myofibers (96, 97). By comparison, mPI damages multiple tissue types, and the death of muscle tissue is accompanied by disruption of arterial supply, venous clearance, and lymphatic drainage. When we stained for iron using Perls' Prussian blue stain, CTX injury did not show detectable levels. Note that Perls' method is only useful for visualizing high levels of iron, as it has a high minimum detection limit and is unable "to detect iron except in massive deposition" (98, 99). Since this threshold was exceeded in mPI but not CTX, we infer that the Mb in CTX injuries must have been cleared before day 3, by mechanisms such as phagocytosis, lymphatics, circulation, and iron homeostasis. In mPI, Perls' stain was positive in both immune cells and extracellular space. Because mPI patients show myoglobin in their urine (19, 59, 60), we infer that a major source of this iron was extracellular myoglobin.

The relative importance of ischemia-reperfusion injury versus deformation injury is a longstanding controversy in the pressure ulcer community. Our finding, that post-pressure intervention can decrease the amount of tissue death, might be interpreted as evidence for the importance of ischemia, but either mechanism is possible. Ischemic damage is usually analysed from the perspective of oxygen and glucose deprivation (blocked influx of beneficial substances), but our results could be understood as failed efflux of deleterious substances (globin/heme/iron). Routes of removal, such as venous and lymphatic drainage, can collapse under much lighter pressure than arterial supply, and this may help explain why serious wounds can arise from light pressure, if sustained over a long duration.

There are several caveats to this work. Mouse wounds differ from human in several obvious ways, such as having denser hair follicle coverage, faster kinetics of DFO, different timing and ratio of phagocytic cells (100), and higher propensity for wound contraction. Although mice can heal skin wounds by contraction, our multi-layer mPI exhibited minimal contraction, as seen from prior work (45) and from the hole in the panniculus muscle layer at day 90. To decrease the impact of hair follicles on results, we placed magnets on regions of skin that were in the resting phase of the hair cycle.

Our experimental design is not capable of distinguishing ischemic from non-ischemic mechanical injuries. Likewise, we cannot distinguish compression-induced pathologies from lysate-induced pathologies. Also, our methods did not distinguish between different iron-containing species such as heme, hemin, free iron, globin protein, and globin cleavage products. Another limitation of our study is

the limited number of myoglobin knockout mice (n = 3) compared with n = 7 for key timepoints of Mb+/+ analysis. This was necessary because Mb unconditional germline knockout had high rates of embryonic lethality. Despite the smaller sample size, several readouts were statistically significant. Another caveat of our study is the use of the panniculus carnosus muscle, which might not generalize to dissimilar muscles (e.g., the upper trochanter). The location of the panniculus carnosus is relevant to heel ulcers (45), and the size was useful for proving that a small amount of muscle damage could disrupt a larger mixed-tissue wound.

Future work should test whether other known phenomena of extracellular hemoglobin are applicable to the extracellular myoglobin of mPI. For example, HO-1 normally detoxifies heme compounds, and its second messenger carbon monoxide might have therapeutic potential for mPI (101). Extracellular hemoglobin and its cleavage products have specific binding sites and innate immune functions relevant to a hemolytic infection (16) and myoglobin should be tested for analogous functions.

Conclusion

Pressure injuries of muscle showed an intrinsically inhospitable microenvironment, and poor regeneration did not require microbial pathogens, diabetes, comorbidities, or old age. Without intervention to improve regeneration, a large gap in the muscle layer remained after 90 days. The initial response to mPI included death of immune cells and failure of phagocytosis, such that layers of necrotic skin, fat, and muscle remained in recognizable layers until they were expelled after two weeks as necroslough, resembling eschar.

Myoglobin iron contributed to the severity, oxidative damage, and delayed healing of mPI. We conclude that the poor healing of mPI shares a mechanistic underpinning with the poor healing of vascular ulcers. mPI research can therefore benefit from the lessons learned in globin overload syndromes such as compartment syndrome, rhabdomyolysis, and hemoglobinopathies. Globin overload occurred in our model, even though the volume of muscle in the wound was far less than the volume of non-muscle tissue.

Targeting myoglobin iron via gene knockout or iron chelation therapy caused an increase in viable immune cells in the wound bed, and revealed a rare instance in where greater number of immune cells correlated with decreased oxidative stress. The increased infiltrate was not sufficient to restore large-scale phagocytosis.

Deferoxamine injections prevented death of tissue at the margins of the wound, when administered starting 12h after pressure was removed. Molecular medicine to block secondary progression is a dramatic new opportunity for pressure injuries, like burns or strokes, to be stabilized shortly after injury, to decrease further loss of salvageable tissue. Deferoxamine injections also led to greater regeneration of muscle and higher quality of muscle, with straighter and more parallel muscle fibers. Straight and parallel fibers improve muscle viability, and healthy muscle will be a crucial defence against recurrence of pressure injuries when the patient eventually puts weight on the same location.

Methods

Mice

Animal experiments were approved by the institutional animal care and use committee (IACUC SHS/2016/1257) of SingHealth, Singapore. To conditionally label Pax7+ muscle satellite stem cells in C57BL6 mice, the Pax7-Cre-ER^{T2} mouse (Jackson Laboratory, ME, USA) was crossed with the Brainbow2.1 (confetti; Jackson Laboratory, ME, USA) mouse. Pax7-Cre-ERT2 provides the Cre-ERT2 transgene downstream of the Pax7 stop codon, thereby limiting the Cre-ERT2 expression to Pax7+ cells. The Cre-ER^{T2} system provides tamoxifen-dependent induction of Cre recombinase, so that affected cells carry heritable rather than transient modification. Upon tamoxifen treatment, the Cre induction causes recombination of the confetti construct at its loxP loci, leading to gene expression of one of the four fluorescent proteins in the construct. The fluorescent proteins are mCerulean (CFP^{mem}), hrGFP II (GFP^{nuc}), mYFP (YFP^{cyt}) and tdimer2(12) (RFP^{cyt}). CFP^{mem} contains a localization sequence enabling its transport to the myofibre membrane (sarcolemma) while GFP^{nuc} contains a nuclear localization sequence. YFP^{cyt} and RFP^{cyt} have no localization sequences and are expected to localize to the cytoplasm. Experimental mice include 5-month-old adult mice and 20-month-old elderly mice.

Myoglobin knockout mice (homozygous in the germline) were created by Cyagen (CA, US) using CRISPR/Cas9 nuclease-mediated genome editing (102, 103). 20-month-old mice (n = 3) were used in the knockout experiments. The myoglobin knockout mice were not injected with tamoxifen.

Mice were euthanized via CO_2 inhalation, followed by cervical dislocation, at timepoints of three, seven, ten, forty, and ninety days following completion of the injury protocol (pressure or toxin). Pressure injury via magnetic compression created two wounds (right and left) on the dorsum of each mouse. Similarly, two cardiotoxin injections were performed on each mouse at the right and left dorsal skinfold. Tissue samples were isolated and one wound tissue (from either pressure or toxin) was fixed in 4% paraformaldehyde at 4°C for eight hours, and then embedded in paraffin. The remaining wound tissue was snap-frozen with isopentane in a liquid nitrogen bath.

Murine pressure injury model

Mice were shaved and remaining hair was removed by hair removal cream (Veet, Singapore) prior to injury. Muscle pressure ulcers were created in 4 to 5-month-old transgenic mice by applying a pair of ceramic magnets (Magnetic Source, Castle Rock, CO, part number: CD14C, grade 8) to the dorsal skinfold. The magnets were 5 mm thick and 12 mm in diameter, with an average weight of 2.7 g and pulling force of 640 g. One of the elderly mice lacked sufficient skinfold for 12 mm magnets, so in that mouse and in its age- and sex-matched control, we used 5 mm magnets (neodymium magnets with a 1 mm spacer on one side; Liftontech Supreme Pte Ltd, Singapore). Because hair follicle (HF) stem cells contribute to wound healing, we attempted to minimize the HF differences by synchronizing the hair growth cycle and applying injury only to skin with HFs in telogen phase (non-pigmented skin). In the case where pigmented skin could not be avoided during magnet placement, i.e. one of the two wounds fell on skin with active hair cycle, that half was excluded from further analysis. Pressure ulcer induction was performed in two cycles. Each cycle was made up of a 12-hour period of magnet placement followed by a 12-hour period without magnets (Suppl. Fig 1A). This procedure induces two pressure wounds on the back of the mouse, on the left and right side of the dorsal skinfold. The dorsal skinfold includes skin, adipose tissue, panniculus carnosus muscle, and loose areolar tissue. The mice were given an analgesic (buprenorphine at 0.1 mg/kg; Bupredyne, Jurox Animal Health, New Zealand) prior to magnet placement and again prior to magnet

removal. Time points post-injury are measured from the end of last magnet cycle. No dressings were used and no debridements were performed.

To treat the pressure injuries, mice were subcutaneously injected with deferoxamine (DFO) while control mice were injected with 0.9% saline (n = 7 each for day 3, 10 and 40 time-points, n = 4 for day 7 and n = 5 for day 90; Suppl. Table 3). The study was initially conducted using 3, 10 and 40 days. When the day 7 and day 90 timepoints were added to the study, we already knew that DFO treatment would give a large effect-size. The updated effect-size caused our power calculation to give a smaller sample-size for day 7 and day 90. The day 7 timepoint was added later because of the dramatic changes observed between day 3 and day 10, and the day 90 timepoint was added later because day 40 mPI showed signs of ongoing regeneration (myoblastic cells and immature myofibers), indicating that steady-state had not yet been reached at day 40.

DFO was administered twice per day at 30mg/kg body weight (or 0.9% saline for control animals) for 16 days, or until mouse sacrifice, whichever was sooner. Under aesthesia, the dorsal skinfold (cranial to the wound) was pulled away from the spine to make a "tent," and the needle was inserted into the tent (over the spine, near the left and right wounds). The first DFO treatment was given 12 hours after completion of the second and final cycle of pressure (Fig 5A). The dosing rationale was as follows: the recommended dose of DFO for iron overload in human patients is 20-60 mg/kg per day (maximum 80 mg/kg; (104)). Mice metabolize DFO faster than humans, so we took the 60 mg/kg per day human dosing and divided it into two half-doses per day.

Murine cardiotoxin injury model

To induce an acute injury in the panniculus carnosus muscle in the skinfold, mice were shaved and fur removed by hair removal cream (Veet, Reckitt, Slough, England) prior to injury. The mice were anaesthetized and 30 µl of toxin at 10 µM concentration was injected intramuscularly into the panniculus carnosus of the dorsal skinfold of each wound (left and right). Because commercial distribution of cardiotoxin from *Naja mossambica* was discontinued, some mice were injected with naniproin instead, while the term "cardiotoxin" has been used for the cohort. Naniproin is a *Naja nigricollis* homologue of cardiotoxin with 95% sequence identity. Naniproin induces myolysis comparable to cardiotoxin. All toxin-injected mice were given an analgesic (buprenorphine at 0.1 mg/kg; Bupredyne, Jurox Animal Health, New Zealand) prior to injection. To control for the post-injury injections given to mPI mice, the toxin-injured mice were injected subcutaneously with 0.9% saline (n = 7) twice daily for 16 days or until mouse sacrifice, whichever was sooner (Suppl. Fig 1B). Tissues were harvested at day 3, 10 or 40 (n = 4). Uninjured healthy tissues were also collected as controls (n = 4).

Histopathology scoring of H&E-stained sections

H&E-stained slides were blinded and scored on the extent of tissue death, immune infiltration, granulation, and regeneration. The scoring for tissue death was defined as follows: 0—healthy tissue with zero or minimal death (< 10% tissue area dead); 1—mild death (11-33%); 2—moderate death (34-67%); 3—extensive tissue death (> 67%). Death was identified by karyolysis, karyorrhexis, and eosinification. Scoring for tissue regeneration was defined as follows: 0 (minimal i.e., < 10% regenerated), 1 (mild i.e., 11-33% regenerated), 2 (moderate i.e., 34-67% regenerated) to 3 (extensive i.e., > 67% regenerated). Scoring for granulation was defined as follows: 0—normal tissue with neither granulation nor neo-angiogenesis; 1—minimal granulation (less than 10% of tissue area); 2—mild granulation (10% to 25% of

tissue area); 3—moderate granulation (26% to 50% of tissue area); 4—high granulation (51% to 75% of tissue area); and 5—extensive granulation (more than 75% of tissue area consisting of granulation tissue). Likewise, the scores for immune infiltration were defined as follows: 0—normal tissue without immune infiltration; 1—minimal immune infiltration (in less than 10% of tissue); 2— mild immune infiltration (in 10% to 25% of tissue); 3—moderate immune infiltration (in 26% to 50% of tissue); 4—high immune infiltration (51% to 75% of tissue area); and 5—extensive immune infiltration (more than 75% of tissue infiltrated by immune cells). Therefore, on the scales for tissue death, regeneration, granulation and immune infiltration, a sample of healthy, uninjured tissue would receive scores of 0, 3, 0, and 0, respectively. Scoring was performed for all treatments and all time-points. The scoring of death, immune infiltration and regeneration was performed for the overall wound and each tissue layer.

Immunofluorescence staining

10 µm fixed paraffin-embedded sections or cryosections were blocked with 10% normal serum and permeabilized with 0.2% Tween 20. Staining was performed using antibodies against 8-Oxoguanine (8-OG or 8-hydroxy-2'-deoxyguanosine; Abcam, Cambridge, UK, ab206461), F4/80 (Abcam, ab6640), Arginase-1 (Arg1; Abcam, Cambridge, UK, ab60176), inducible nitric oxide synthase (iNOS; Cell Signalling Technology, MA, USA, #13120), citrullinated histone H3 (citH3; Abcam, ab5103), nitrotyrosine (NTYR; Abcam, Cambridge, UK, ab7048), and myoglobin (Cell Signalling Technology, MA, USA; 25919S). For detection, we used Alexa-Fluor 488-, 594- and 647-conjugated secondary antibodies (Abcam, Cambridge, UK, ab150129, ab150064, ab150075 respectively) raised in appropriate species for the experiments. The slides were mounted with Vectashield Hardset with DAPI (Vector Laboratories, CA, USA) and images were acquired on a Leica TCS SP8 confocal microscope (Leica Microsystems, Wetzlar, Germany) and analysed using LAS X software. For quantification, the number of fluorescence-positive pixels of each 512 x 512 frame was measured using Adobe Photoshop (Adobe Inc., CA, USA). In other words, the quantification covers all layers of the wound, and text description is added if specific layers were disproportionately responsible.

Statistical analyses

For single comparisons, statistical significance was computed using an unpaired two-tailed Student's t test. For multiple comparisons, a one-way ANOVA (analysis of variance) was followed by the Tukey post-hoc test, except for the Luminex assays (Supplementary Tables 2 and 4), which were analyzed by two-way ANOVA for treatment and analyte. Tests and plots were generated by GraphPad Prism (version 9.0.0 for Windows, GraphPad Software, CA, USA). An asterisk (*) refers to a p value less than 0.05, (**) means $p < 0.01$, (***) means $p < 0.001$ and (****) means $p < 0.0001$. "ns" means not significant.

Author contributions

NJMN: Investigation, Data analysis, Writing. JH: Methodology, Investigation. JHJ: Investigation, Project administration. NHH: Sample processing. RB: Methodology. PTS: Supervision. LTK: Conceptualization, Funding acquisition, Supervision, Writing.

Acknowledgements

We acknowledge funding from the Singapore Ministry of Health's National Medical Research Council (NMRC/OFIRG/0007/2016), and also from the Singapore Ministry of Education's Tier2 Grant (MOE2019-T2-1-138) and the National Research Foundation, Prime Minister's Office, Singapore under its Campus for Research Excellence and Technological Enterprise (CREATE) programme, through Singapore MIT Alliance for Research and Technology (SMART): Critical Analytics for Manufacturing Personalised-Medicine (CAMP) Inter-Disciplinary Research Group.

We thank Manjunatha Kini and Koh Cho Yeow for naniproin; Ann-Marie Chacko and Tham Jing Yang for detection methods; N. Suhas Jagannathan for image analysis; Sng Kian Boon Colin for some HO-1 images; Aadya S. Deshpande for repeated assistance; Paul Matsudaira, Jasmine Chin, Mynn Varela, Ruklanthi de Alwis, the Mechanobiology Institute (Singapore) Microscopy facility, and the SingHealth Advanced BioImaging facility for advice.

References

1. Girouard K, et al. The symptom of pain with pressure ulcers: a review of the literature. *Ostomy Wound Manage.* 2008;54(6):8.
2. Padula WV, Delarmente BA. The national cost of hospital-acquired pressure injuries in the United States. *Int Wound J.* 2019;16(3):634-40.
3. Wassel CL, et al. Risk of readmissions, mortality, and hospital-acquired conditions across hospital-acquired pressure injury (HAPI) stages in a US National Hospital Discharge database. *Int Wound J.* 2020;17(6):1924-34.
4. Gray RJ, Voegeli D, Bader DL. Features of lymphatic dysfunction in compressed skin tissues - Implications in pressure ulcer aetiology. *J Tissue Viability.* 2016;25(1):26-31.
5. Mervis JS, Phillips TJ. Pressure ulcers: Prevention and management. *J Am Acad Dermatol.* 2019;81(4):893-902.
6. Bouten CV, et al. The etiology of pressure ulcers: skin deep or muscle bound? *Arch Phys Med Rehabil.* 2003;84(4):616-9.
7. Preston A, et al. Deep tissue pressure injury: A clinical review. *Am J Nurs.* 2017;117(5):50-7.
8. Goldman DW, et al. Acellular hemoglobin-mediated oxidative stress toward endothelium: a role for ferryl iron. *Am J Physiol.* 1998;275(3):H1046-53.
9. Reeder BJ, Wilson MT. Hemoglobin and myoglobin associated oxidative stress: from molecular mechanisms to disease states. *Curr Med Chem.* 2005;12(23):2741-51.
10. Kato GJ, et al. Intravascular hemolysis and the pathophysiology of sickle cell disease. *J Clin Invest.* 2017;127(3):750-60.
11. Nader E, et al. The Red Blood Cell-Inflammation Vicious Circle in Sickle Cell Disease. *Front Immunol.* 2020;11(454).
12. Mendonça R, et al. Red cell DAMPs and inflammation. *Inflamm Res.* 2016;65(9):665-78.
13. Bozza MT, Jeney V. Pro-inflammatory actions of heme and other hemoglobin-derived DAMPs. *Front Immunol.* 2020;11:1323.
14. Bogdan, C. Oxidative burst without phagocytes: the role of respiratory proteins. *Nat Immunol.* 2007;8:1029–31.
15. Jiang N, et al. Respiratory protein–generated reactive oxygen species as an antimicrobial strategy. *Nat Immunol.* 2007;8:1114-22.
16. Bahl N, et al. Extracellular haemoglobin upregulates and binds to tissue factor on macrophages: implications for coagulation and oxidative stress. *Thromb Haemost.* 2014;111(1):67-78.
17. Bahl N, et al. Delineation of lipopolysaccharide (LPS)-binding sites on hemoglobin: from in silico predictions to biophysical characterization. *J Biol Chem.* 2011;286(43):37793-803.
18. BJ., Cherayil. The role of iron in the immune response to bacterial infection. *Immunol Res.* 2011;50(1):1-9.
19. Traa WA, et al. Myoglobin and troponin concentrations are increased in early stage deep tissue injury. *J Mech Behav Biomed Mater.* 2019;92:50-7.
20. Makhsous M, et al. Elevation in the serum and urine concentration of injury-related molecules after the formation of deep tissue injury in a rat spinal cord injury pressure ulcer model. *PM R.* 2010;2(11):1063-5.
21. Loerakker S, et al. Plasma variations of biomarkers for muscle damage in male nondisabled and spinal cord injured subjects. *J Rehabil Res Dev.* 2012;49(3):361-72.
22. Reeder BJ, et al. Iron chelators can protect against oxidative stress through ferryl heme reduction. *Free Radic Biol Med.* 2008;44(3):264-73.
23. Rojkind M, et al. Role of hydrogen peroxide and oxidative stress in healing responses. *Cell Mol Life Sci.* 2002;59(11):1872-91.

24. Kapralov A, et al. Peroxidase activity of hemoglobin-haptoglobin complexes: covalent aggregation and oxidative stress in plasma and macrophages. *J Biol Chem.* 2009;284(44):30395-407.
25. Plotnikov EY, et al. Myoglobin causes oxidative stress, increase of NO production and dysfunction of kidney's mitochondria. *Biochim Biophys Acta.* 2009;1792(8):796-803.
26. Osawa Y, Williams MS. Covalent crosslinking of the heme prosthetic group to myoglobin by H2O2: toxicological implications. *Free Radic Biol Med* 1996;21(1):35-41.
27. Boutaud O, Roberts LJ 2nd. Mechanism-based therapeutic approaches to rhabdomyolysis-induced renal failure. *Free Radic Biol Med.* 2011;51(5):1062-7.
28. Dixon SJ, et al. Ferroptosis: an iron-dependent form of nonapoptotic cell death. *Cell.* 2012 149(5):1060-72.
29. Velasquez J, Wray AA. *Deferoxamine.* Treasure Island (FL): StatPearls Publishing; 2021 May 31.
30. Karnon J, et al. Lifetime cost-utility analyses of deferasirox in beta-thalassaemia patients with chronic iron overload: a UK perspective. *Clin Drug Investig.* 2012;32(12):805-15.
31. Morel I, et al. Antioxidant and free radical scavenging activities of the iron chelators pyoverdin and hydroxypyrid-4-ones in iron-loaded hepatocyte cultures: comparison of their mechanism of protection with that of desferrioxamine. *Free Radic Biol Med.* 1992;13(5):499-508.
32. Vanek T, Kohli A. *Biochemistry, Myoglobin.* Treasure Island (FL): StatPearls Publishing; 2021.
33. Xiao H, et al. The possible mechanisms underlying the impairment of HIF-1α pathway signaling in hyperglycemia and the beneficial effects of certain therapies. *Int J Med Sci.* 2013;10(10):1412-21.
34. Duscher D, et al. Transdermal deferoxamine prevents pressure-induced diabetic ulcers. *PNAS.* 2015;112(1):94-9.
35. Holden P, Nair LS. Deferoxamine: An angiogenic and antioxidant molecule for tissue regeneration. *Tissue Eng Part B Rev.* 2019;25(6):461-70.
36. Jagannathan NS, Tucker-Kellogg L. Membrane permeability during pressure ulcer formation: A computational model of dynamic competition between cytoskeletal damage and repair. *J Biomech.* 2016;49(8):1311-20.
37. Stadler I, et al. Development of a simple, noninvasive, clinically relevant model of pressure ulcers in the mouse. *Journal of Investigative Surgery.* 2004;17(4):221-7.
38. European Pressure Ulcer Advisory Panel, National Pressure Injury Advisory Panel, Pan Pacific Pressure Injury Alliance. *Prevention and treatment of pressure ulcers/injuries: Clinical practice guideline. The international guideline.* EPUAP/NPIAP/PPPIA; 2019.
39. Ferris AE, Harding KG. An overview of the relationship between anaemia, iron, and venous leg ulcers. *Int Wound J.* 2019;16(6):1323-9.
40. Sindrilaru A, et al. An unrestrained proinflammatory M1 macrophage population induced by iron impairs wound healing in humans and mice. *J Clin Invest.* 2011;121(3):985-97.
41. Ballart IJ, et al. Progressive dysfunction of monocytes associated with iron overload and age in patients with thalassemia major. *Blood.* 1986;67(1):105-9.
42. Liu YY, et al. Elevated heme impairs macrophage phagocytosis in endometriosis. *Reproduction.* 2019;158(3):257-66.
43. Martins R, et al. Heme drives hemolysis-induced susceptibility to infection via disruption of phagocyte functions. *Nat Immunol.* 2016;12:1361-72.
44. McGuire JB, Nasser JJ. *Symposium on Advanced Wound Care*. Las Vegas, Nevada, USA: HMP Global Learning Network; 2019.
45. Nasir NJM, et al. The panniculus carnosus muscle: a missing link in the chronicity of heel pressure ulcers? *J R Soc Interface.* 2021;19:1920210631.

46. Kristiansen M, et al. Identification of the haemoglobin scavenger receptor. *Nature.* 2001;409(6817):198-201.
47. Soares MP, Hamza I. Macrophages and iron metabolism. *Immunity.* 2016;44(3):492-504.
48. Bessman NJ, et al. Dendritic cell-derived hepcidin sequesters iron from the microbiota to promote mucosal healing. *Science.* 2020;368(6487):186-9.
49. Chen G, et al. Heme-induced neutrophil extracellular traps contribute to the pathogenesis of sickle cell disease. *Blood.* 2014;123(24):3818-27.
50. Okubo K, Ket al. Macrophage extracellular trap formation promoted by platelet activation is a key mediator of rhabdomyolysis-induced acute kidney injury. *Nat Med.* 2018;24(2):232–8.
51. Ohbuchi A, et al. Quantitative analysis of hemin-induced neutrophil extracellular trap formation and effects of hydrogen peroxide on this phenomenon. *Biochem Biophys Rep.* 2017;11:147-53.
52. B., Halliwell. Artefacts with ascorbate and other redox-active compounds in cell culture: epigenetic modifications, and cell killing due to hydrogen peroxide generation in cell culture media. *Free Radic Res.* 2018;52(9):907-9.
53. Tucker-Kellogg L, et al. Reactive oxygen species (ROS) and sensitization to TRAIL-induced apoptosis, in Bayesian network modelling of HeLa cell response to LY303511. *Biochem Pharmacol.* 2012;84(10):1307-17.
54. Garry DJ, et al. Mice without myoglobin. *Nature.* 1998;395(6705):905-8.
55. Gödecke A, et al. Disruption of myoglobin in mice induces multiple compensatory mechanisms. *Proc Natl Acad Sci.* 1999;96(18):10495-500.
56. Meeson AP, et al. Adaptive mechanisms that preserve cardiac function in mice without myoglobin. *Circ Res.* 2001;88(7):713-20.
57. Ma KL, et al. Activation of the CXCL16/CXCR6 pathway promotes lipid deposition in fatty livers of apolipoprotein E knockout mice and HepG2 cells. *Am J Transl Res.* 2018;10(6):1802-16.
58. Tierney MT, et al. Muscle stem cells exhibit distinct clonal dynamics in response to tissue repair and homeostatic aging. *Cell Stem Cell.* 2018;22(1):119-27.
59. WA, Traa. Technische Universiteit Eindhoven; 2019:140.
60. JM, Levine. Rhabdomyolysis in association with acute pressure sore. *J Am Geriatr Soc.* 1993;41(8):870-2.
61. Kilinc K, et al. Myoglobin-catalyzed tyrosine nitration: no need for peroxynitrite. *Biochem Biophys Res Commun.* 2001;285(2):273-6.
62. S., Herold. Nitrotyrosine, dityrosine, and nitrotryptophan formation from metmyoglobin, hydrogen peroxide, and nitrite. *Free Radic Biol Med.* 2004;36(5):565-79.
63. Schlieper G, et al. Adaptation of the myoglobin knockout mouse to hypoxic stress. *Am J Physiol Regul Integr Comp Physiol.* 2004;286(4):R786-92.
64. Moynié L, et al. The complex of ferric-enterobactin with its transporter from Pseudomonas aeruginosa suggests a two-site model. *Nat Commun* 2019;10:3673.
65. Li J, et al. Ferroptosis: past, present and future. *Cell Death Dis.* 2020;11(2):88.
66. Li S, et al. Diabetic ferroptosis plays an important role in triggering on inflammation in diabetic wound. *Am J Physiol Endocrinol Metab.* 2021;213(4):E509-E20.
67. Kao JK, et al. Chronic iron overload results in impaired bacterial killing of THP-1 derived macrophage through the inhibition of lysosomal acidification. *PLoS One.* 2016;11(5):e0156713.
68. van Asbeck BS, et al. Functional defects in phagocytic cells from patients with iron overload. *J Infect.* 1984;8(3):232-40.
69. Porto G, De Sousa M. Iron overload and immunity. *World J Gastroenterol.* 2007;13(35):4707-15.
70. Cantinieaux B, et al. Neutrophil dysfunctions in thalassaemia major: The role of cell iron overload. *Eur J Haematol.* 1987;39(1):28-34.
71. Grey JE, et al. Wound assessment. *BMJ.* 2006;332(7536).

72. JB, McGuire. *APMA Annual Scientific Meeting*. Salt Lake City, Utah, USA: American Podiatric Medical Association; 2019.
73. Manna B, et al. *Wound Debridement.* Treasure Island (FL): StatPearls Publishing; 2021.
74. Bluestein D, Javaheri A. Pressure ulcers: prevention, evaluation, and management. *Am Fam Physician.* 2008;78(10):1186-94.
75. Raetz JGM, Wick KH. Common questions about pressure ulcers. *Am Fam Physician.* 2015;92(10):888-94.
76. Strowitzki MJ, et al. Protein hydroxylation by hypoxia-inducible factor (HIF) hydroxylases: unique or ubiquitous? *Cells.* 2019;8(5):384.
77. Hazarika S, et al. Myocyte specific overexpression of myoglobin impairs angiogenesis after hind-limb ischemia. *Arterioscler Thromb Vasc Biol.* 2008;28(12).
78. Meisner JK, et al. Myoglobin overexpression inhibits reperfusion in the ischemic mouse hindlimb through impaired angiogenesis but not arteriogenesis. *Am J Pathol.* 2013;183(6):1710-8.
79. Handa P, et al. Iron alters macrophage polarization status and leads to steatohepatitis and fibrogenesis. *J Leukoc Biol.* 2019;105(5):1015-26.
80. Agoro R, et al. Cell iron status influences macrophage polarization. *PLoS One.* 2018;13(5):e0196921.
81. Ali MK, et al. Critical role for iron accumulation in the pathogenesis of fibrotic lung disease. *J Pathol.* 2020;251(1):49-62.
82. Eriksson A, et al. Hypertrophic muscle fibers with fissures in power-lifters; fiber splitting or defect regeneration? . *Histochem Cell Biol.* 2006;126(4):409-17.
83. Pichavant C, et al. Decrease of myofiber branching via muscle-specific expression of the olfactory receptor mOR23 in dystrophic muscle leads to protection against mechanical stress. *Skelet Muscle.* 2016;6(2).
84. González-Montero J, et al. Myocardial reperfusion injury and oxidative stress: Therapeutic opportunities. *World J Cardiol.* 2018;10(9):74-86.
85. Morris SF, et al. Deferoxamine attenuates ischemia-induced reperfusion injury in the skin and muscle of myocutaneous flaps in the pig. *Plast Reconstr Surg.* 1993;92(1):120-32.
86. Yang L, et al. Deferoxamine Treatment Combined With Sevoflurane Postconditioning Attenuates Myocardial Ischemia-Reperfusion Injury by Restoring HIF-1/BNIP3-Mediated Mitochondrial Autophagy in GK Rats. *Front Pharmacol.* 2020;11:6.
87. Strong AL, et al. Characterization of a murine pressure ulcer model to assess efficacy of adipose-derived stromal cells. *Plast Reconstr Surg Glob Open.* 2015;3(3):e334.
88. Ahmed AK, et al. A non-invasive method to produce pressure ulcers of varying severity in a spinal cord-injured rat model. *Spinal Cord.* 2016;54(12):1096-104.
89. Siu PM, et al. Muscle apoptosis is induced in pressure-induced deep tissue injury. *J Appl Physiol.* 1985;107(4):1266-75.
90. Wassermann E, et al. A chronic pressure ulcer model in the nude mouse. *Wound Repair Regen.* 2009;17(4):480-4.
91. Salcido R, et al. Histopathology of pressure ulcers as a result of sequential computer-controlled pressure sessions in a fuzzy rat model. *Adv Wound Care.* 1994;7(5):23-4.
92. Salcido R, et al. Animal models in pressure ulcer research. *J Spinal Cord Med.* 2007;30(2):107-16.
93. Hickle K, et al. Wireless Pressure Ulcer Sensor: Validation in an Animal Model. *Ann Plast Surg.* 2019;82(4S Suppl 3):S215-S21.
94. Cichowitz A, et al. . The heel: anatomy, blood supply, and the pathophysiology of PUs. *Ann Plast Surg* 2009;62(4):423e9.
95. Soh WSB, et al. *Innovations and Emerging Technologies in Wound Care*. Elsevier; 2020:41-52.

96. Guardiola O, et al. Induction of acute skeletal muscle regeneration by cardiotoxin injection. *J Vis Exp.* 2017(119):e54515.
97. Harvey AL, et al. Effects of purified cardiotoxins from the Thailand cobra (Naja naja siamensis) on isolated skeletal and cardiac muscle preparations. . *Toxicon.* 1982;20(2).
98. Perl DP, Good PF. Comparative techniques for determining cellular iron distribution in brain tissues. *Ann Neurol.* 1992;32:S76-81.
99. Liu S, et al. Comparative analysis of H&E and Prussian blue staining in a mouse model of cerebral microbleeds. *J Histochem Cytochem.* 2014;62(11).
100. Zomer HD, Trentin AG. Skin wound healing in humans and mice: Challenges in translational research. *J Dermatol Sci.* 2018;90(1):3-12.
101. Motterlini R, Otterbein L. The therapeutic potential of carbon monoxide. *Nat Rev Drug Discov.* 2010;9(9):728-43.
102. Qin W, et al. Efficient CRISPR/Cas9-mediated genome editing in mice by zygote electroporation of nuclease. *Genetics.* 2015;200(2):423-30.
103. Qin W, et al. Generating mouse models using CRISPR-Cas9-mediated genome editing. *Curr Protoc Mouse Biol.* 2016;6(1):39-66.
104. Barata JD, et al. Low-dose (5 mg/kg) desferrioxamine treatment in acutely aluminium-intoxicated haemodialysis patients using two drug administration schedules. *Nephrol Dial Transplant.* 1996;11(1):125-32.

Figure legends

Figure 1: Poor regeneration of muscle pressure injury (mPI), a model of chronic wound, compared with cardiotoxin (CTX), a model of acute injury. H&E-stained sections of wound tissues (A-B) at day 10 post-injury and (C-D) day 40 post-injury. Red arrows point to the panniculus carnosus layer. '+' indicates where the panniculus layer should be. Scale bars: 50 µm. Uninjured control tissue, stained with H&E, is shown in Suppl. Fig 1C. (E) Full cross-section of H&E-stained mPI, including uninjured edges, at day 10 post-injury. Note the eschar attached to the wound surface. Scale bar: 500 µm. (F-G) Comparison of the regeneration scores for the panniculus layer between mPI and CTX injuries at day 10 and day 40. (H) A multi-channel confocal image of the panniculus layer shows a round hole remains in the muscle, 90 days after mPI. Scale bar: 1000 µm.

Figure 2: Early-stage pathologies in the injury-response of mPI (3 days after injury). (A-B) H&E-stained sections of wound tissues, comparing magnet-induced mPI versus cardiotoxin (CTX) injury. Red arrows point to the panniculus carnosus (PC) layer. (C) Thickness of PC layer. (D) Histopathology scoring of immune infiltrate into the injured PC layer. (E-F) Immuno-staining for citrullinated histone-3 (CitH3, a marker for extracellular traps, in red) in mPI versus CTX. DNA/nuclei were co-stained blue with DAPI. (G) Quantification of CitH3 staining. (H-I) Perls' Prussian blue iron staining (dark blue-grey), with nuclear fast red co-stain. (J) Quantification of Perls' staining. (K-L) Immuno-staining for heme oxygenase-1 (HO-1, a marker of heme and iron) in mPI versus CTX. Note that the HO-1 positive signal in CTX injury is localized to the panniculus carnosus, and is widespread across all layers in mPI. Scale bars: 50 µm. (M) Quantification of HO-1 staining.

Figure 3: Myoglobin knockout decreased iron deposits and tissue death after mPI. (A-B) Perls' Prussian blue iron staining. (A) Note iron deposits in the extracellular space and in immune cells of Mb+/+ wound tissue, and note that (B) Mb−/− tissues have no iron deposits in extracellular regions. (C) Quantification of Perls' staining. (D-E) Immuno-staining for HO-1 in Mb+/+ versus Mb−/− tissues at day 3 after mPI. Note that HO-1 is elevated in all layers of Mb−/− except epidermis. (F) Quantification of HO-1 immuno-staining. (G-H) H&E-stained sections of Mb+/+ versus Mb−/− mPI. Paraffin-embedded wound sections derived from elderly Mb-wildtype mice had poor cohesiveness (compared to elderly Mb-knockout or young) and exhibited greater cracking during identical sample handling. (I) Amount of immune infiltrate, quantified by histopathology scoring on a scale of 0 to 5, performed on day 3 sections. (J) External wound area in Mb+/+ and −/− mice in the initial days following mPI from 12 mm magnets. Statistical analysis compared four wounds from two age- and sex-matched animals using a Student's t test for each day. Consistent with these results, Suppl. Table 1 shows additional animals treated with different-sized magnets. (K) Tissue death in the PC muscle layer by histopathology scoring (3 indicates pervasive death).

Figure 4: Myoglobin knockout caused a more hospitable wound environment in mPI. (A-D) Immunostaining of 8-oxaguanine (8-OG; in magenta) in Mb+/+ versus Mb−/− mPI. Nuclei were co-stained blue with DAPI. (B) and (D) are bright-field images of (A) and (C), respectively. (E) Quantification of 8-OG staining. (F-I) BODIPY staining (for lipid peroxidation) in Mb+/+ versus Mb−/−. (G) and (I) are bright-field images of (F) and (H), respectively. (J) Quantification of BODIPY staining. (K-P) Immuno-staining for CitH3 (in red) in Mb+/+ versus Mb−/−. (L, O) DNA/nuclei were co-stained blue with DAPI. (M) and (P) are bright-field images of (K) and (N), respectively. Scale bars: 50 µm. (Q) Quantification of CitH3 staining.

Figure 5: Deferoxamine (DFO) iron chelation therapy decreased iron deposits at day 3 after mPI. (A) Experimental schedule shows confetti fluorescence induction via tamoxifen, mPI induction, treatment

with DFO or saline, and tissue harvest. (B) Diameter of the dead region of the panniculus carnosus (PC) muscle in tissue sections from DFO- versus saline-treated mPI, 3 days post-injury. (C-D) Perls' Prussian blue iron staining of (C) saline-treated, and (D) DFO-treated wounds. (E) Quantification of Perls' staining. (F-G) Immunostaining of HO-1 in saline- and DFO-treated. (H) Quantification of HO-1 staining. (I-J) H&E-stained sections of saline- versus DFO-treated mPI at the wound center. (K) Histopathology scoring of immune infiltrate throughout the wound at day 3 between saline- and DFO-treated mPI. (L) Confirmation that injuries were created, according to death of PC tissue at the center of the wound (histopathology scoring where 3 indicates pervasive tissue death). (M) Skin wound area in saline- and DFO-treated mice following mPI.

Figure 6: DFO treatment improved the mPI microenvironment (day 3). (A-D) Immunostaining of 8-OG (for DNA damage) in saline-treated versus DFO-treated mPI. Nuclei were stained blue with DAPI. (B) and (D) are bright-field images of (A) and (C), respectively. (E) Quantification of 8-OG. (F-I) BODIPY staining (for lipid peroxidation) and brightfield in saline- versus DFO-treated mPI. (J) Quantification of BODIPY. (K-P) CitH3 immuno-staining with DNA/nuclear co-stain and brightfield in saline- versus DFO-treated mPI. Scale bars: 50 µm. (Q) Quantification of CitH3 staining.

Figure 7: DFO treatment improved immune infiltration (7 and 10 days after mPI). (A-B) Immuno-staining of inducible nitric oxide synthase (iNOS, associated with pro-inflammatory activation) in saline- versus DFO-treated mPI at day 7 post-injury. (C-D) Nuclei are stained blue with DAPI, to show the count of infiltrating cells. (E-F) Immuno-staining of Arginase-1 in saline- versus DFO-treated mPI at day 10 post-injury. (G-H) Nuclei are co-stained blue with DAPI. (I-J) Merged brightfield and Arg-1 immuno-staining. Scale bars: 100 µm. (K) Quantification of iNOS staining at day 7 between saline- and DFO-treated. (L) Scoring of immune infiltrate into the injured tissue at day 7. (M) Scoring of immune infiltrate into the injured tissue at day 10. (N) Quantification of Arg-1 staining. (O) Quantification of DAPI staining. (P) Distance of tissue infiltrated by Arg-1+ cells in saline- versus DFO-treated tissues.

Figure 8: DFO increased the extent of muscle regeneration at day 40 & day 90. (A-B) Confocal fluorescent and (C-D) H&E-stained cross-sections of regenerated muscle fibers from saline- and DFO-treated mPI, 40 days post-injury. Scale bars: 100 µm. (E-F) Histological scoring of PC muscle regeneration in saline- and DFO-treated mPI versus acute CTX-injured tissues at the center and edge of the wound, 40 days post-injury. (G) Diameter of gap (unregenerated region) in PC muscle layer at day 90 post-mPI between saline- and DFO-treated wounds.

Figure 9: DFO improved muscle morphology. Confocal microscopy of confetti labelled muscle regeneration in ex vivo tissue blocks. Note that unlabelled tissue types such as blood vessels and hair create black shadows on top of the images. (A-C) Left column shows healthy regeneration in the control condition, toxin-induced injury, at 40 days. Experiment was halted at 40 days due to complete regeneration. (D-F) Middle column shows regenerated muscle fibers of saline-treated mPI, 90 days post-injury. Note the presence of non-parallel fibers, bent fibers, and split fibers (i.e., fibers with one or more branches). (G-I) Right column shows regenerated muscle fibers of DFO-treated mPI, 90 days post-injury. Scale bar: 100 µm. (J) Quantification of muscle fiber malformations.

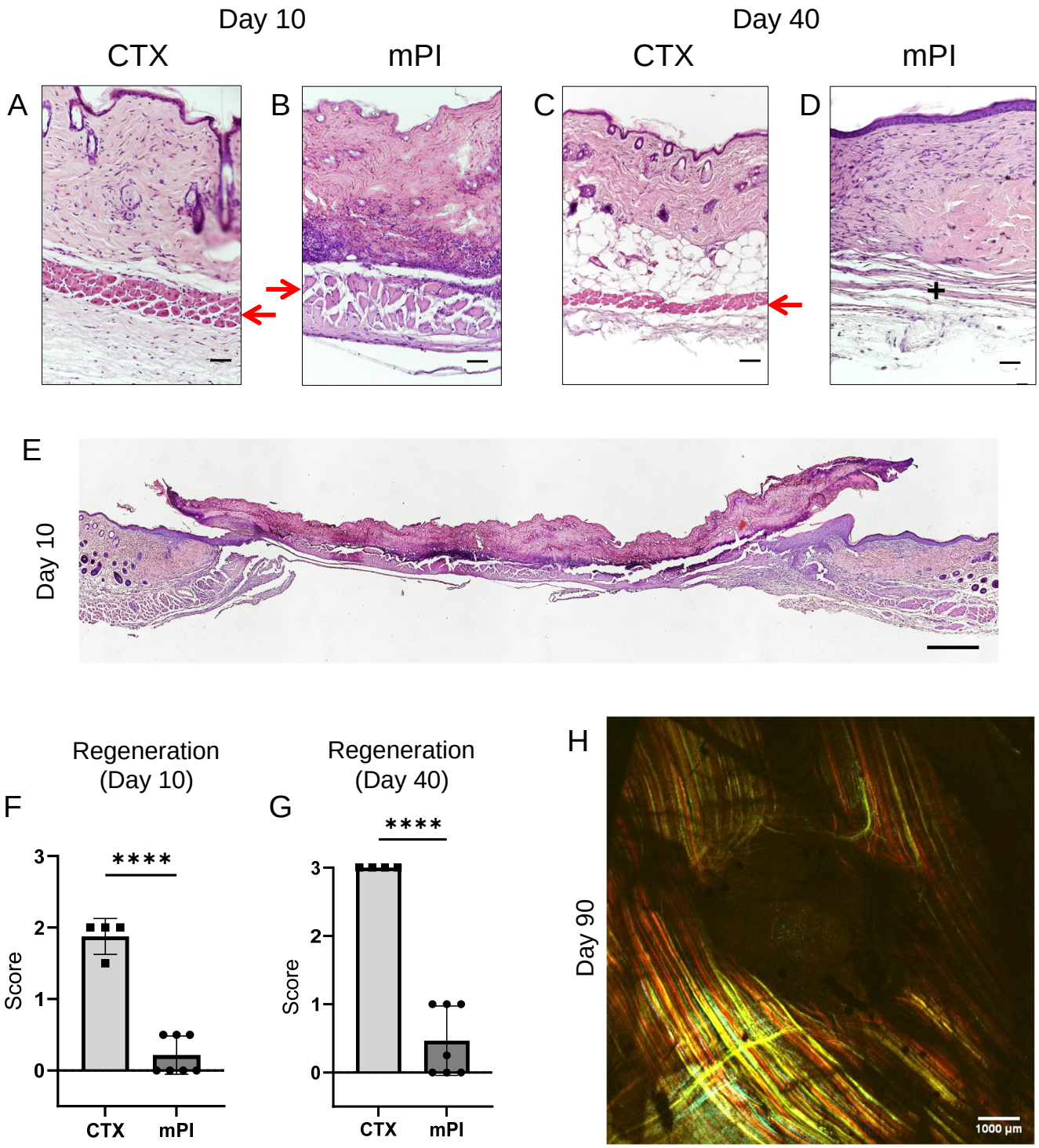

Figure 1: Poor regeneration of muscle pressure injury (mPI), a model of chronic wound, compared with cardiotoxin (CTX), a model of acute injury. H&E-stained sections of wound tissues (A-B) at day 10 post-injury and (C-D) day 40 post-injury. Red arrows point to the panniculus carnosus layer. '+' indicates where the panniculus layer should be. Scale bars: 50 µm. Uninjured control tissue, stained with H&E, is shown in Suppl. Fig 1C. (E) Full cross-section of H&E-stained mPI, including uninjured edges, at day 10 post-injury. Note the eschar attached to the wound surface. Scale bar: 500 µm. (F-G) Comparison of the regeneration scores for the panniculus layer between mPI and CTX injuries at day 10 and day 40. (H) A multi-channel confocal image of the panniculus layer shows a round hole remains in the muscle, 90 days after mPI. Scale bar: 1000 µm.

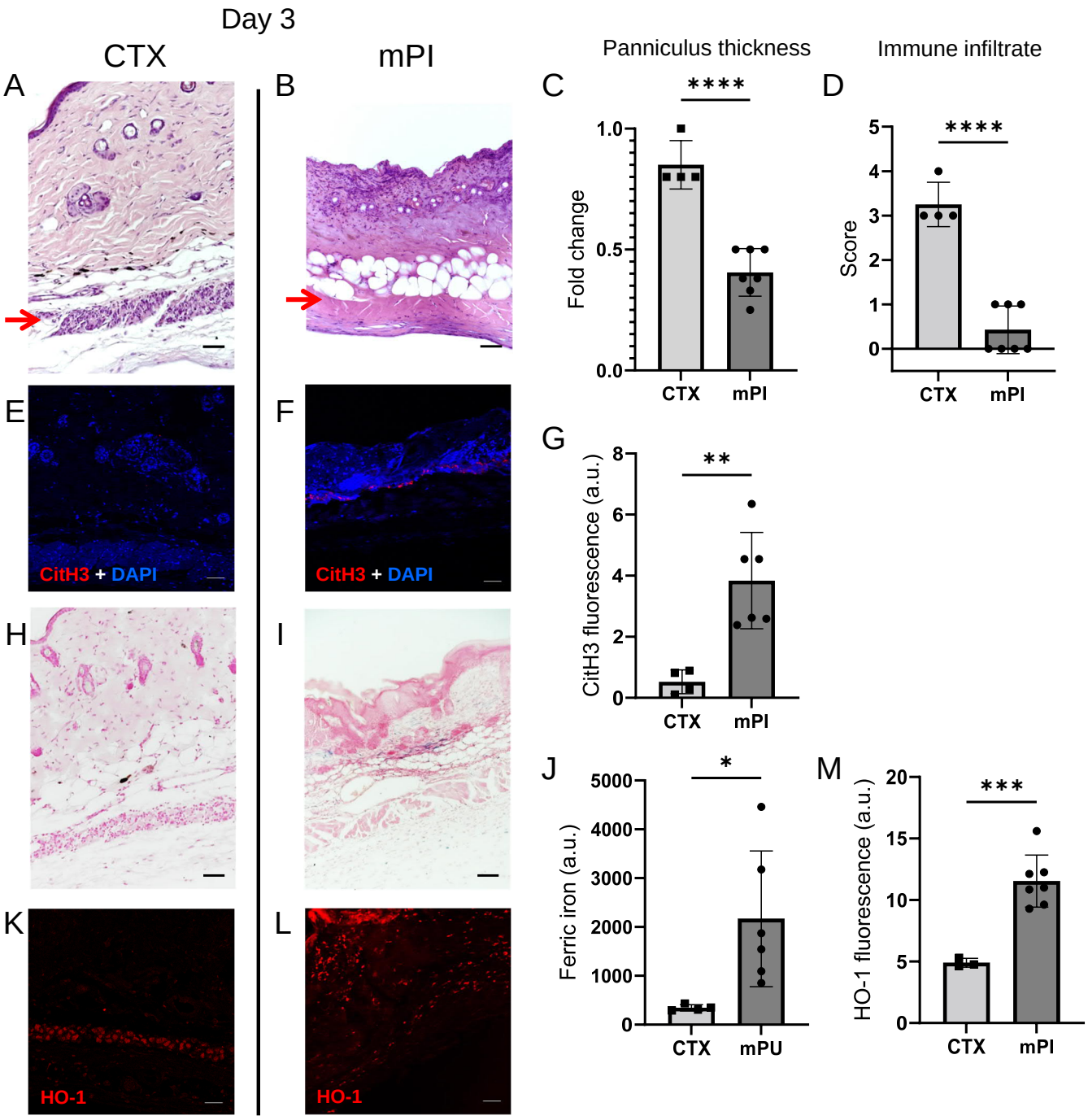

Figure 2: Early-stage pathologies in the injury-response of mPI (3 days after injury). (A-B) H&E-stained sections of wound tissues, comparing magnet-induced mPI versus cardiotoxin (CTX) injury. Red arrows point to the panniculus carnosus (PC) layer. (C) Thickness of PC layer. (D) Histopathology scoring of immune infiltrate into the injured PC layer. (E-F) Immuno-staining for citrullinated histone-3 (CitH3, a marker for extracellular traps, in red) in mPI versus CTX. DNA/nuclei were co-stained blue with DAPI. (G) Quantification of CitH3 staining. (H-I) Perls' Prussian blue iron staining (dark blue-grey), with nuclear fast red co-stain. (J) Quantification of Perls' staining. (K-L) Immuno-staining for heme oxygenase-1 (HO-1, a marker of heme and iron) in mPI versus CTX. Note that the HO-1 positive signal in CTX injury is localized to the panniculus carnosus, and is widespread across all layers in mPI. Scale bars: 50 µm. (M) Quantification of HO-1 staining.

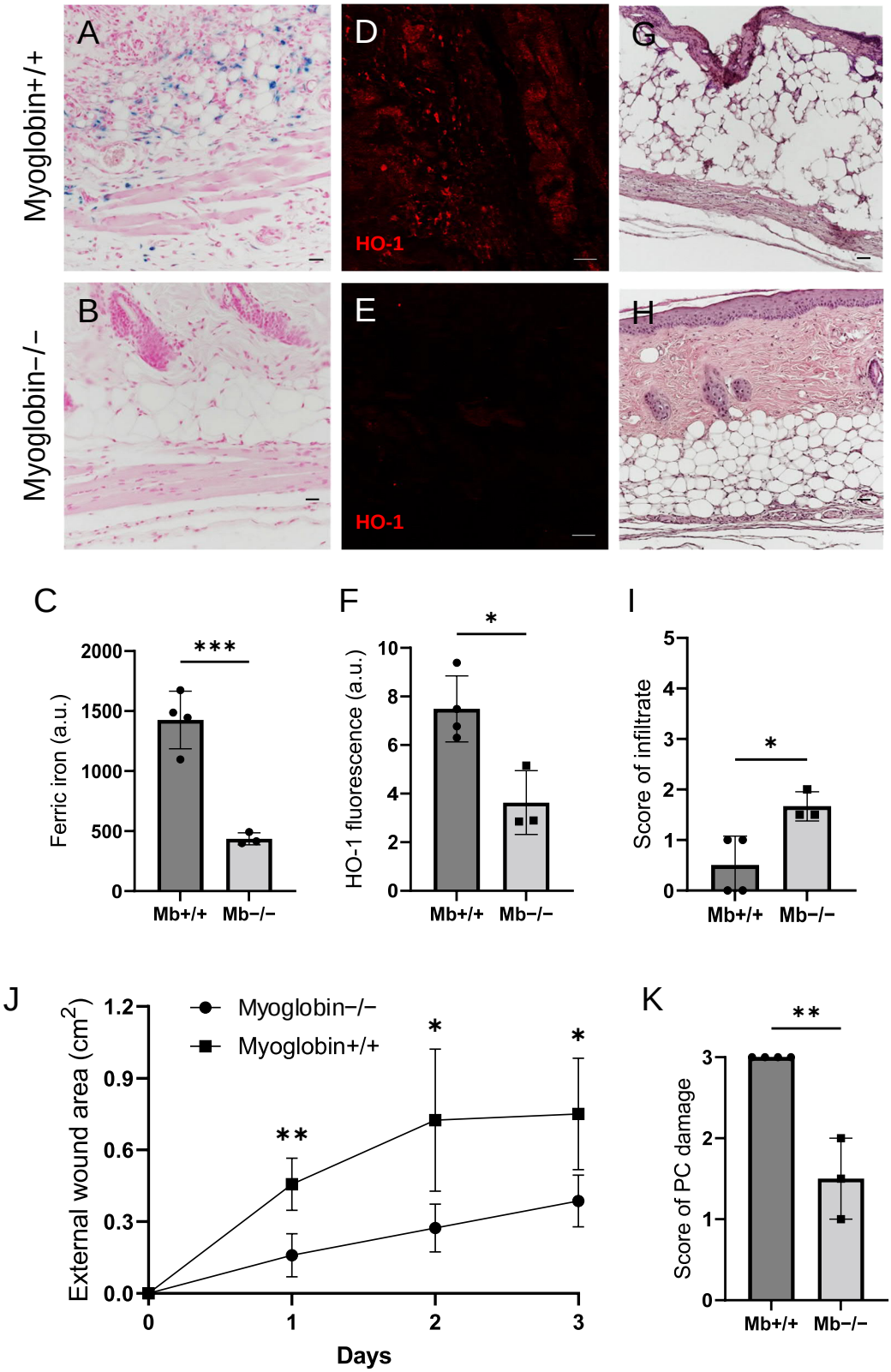

Figure 3: Myoglobin knockout decreased iron deposits and tissue death after mPI. (A-B) Perls' Prussian blue iron staining. (A) Note iron deposits in the extracellular space and in immune cells of Mb+/+ wound tissue, and note that (B) Mb−/− tissues have no iron deposits in extracellular regions. (C) Quantification of Perls' staining. (D-E) Immuno-staining for HO-1 in Mb+/+ versus Mb−/− tissues at day 3 after mPI. Note that HO-1 is elevated in all layers of Mb−/− except epidermis. (F) Quantification of HO-1 immuno-staining. (G-H) H&E-stained sections of Mb+/+ versus Mb−/− mPI. Paraffin-embedded wound sections derived from elderly Mb-wildtype mice had poor cohesiveness (compared to elderly Mb-knockout or young) and exhibited greater cracking during identical sample handling. (I) Amount of immune infiltrate, quantified by histopathology scoring on a scale of 0 to 5, performed on day 3 sections. (J) External wound area in Mb+/+ and −/− mice in the initial days following mPI from 12 mm magnets. Statistical analysis compared four wounds from two age- and sex-matched animals using a Student's t test for each day. Consistent with these results, Suppl. Table 1 shows additional animals treated with different-sized magnets. (K) Tissue death in the PC muscle layer by histopathology scoring (3 indicates pervasive death).

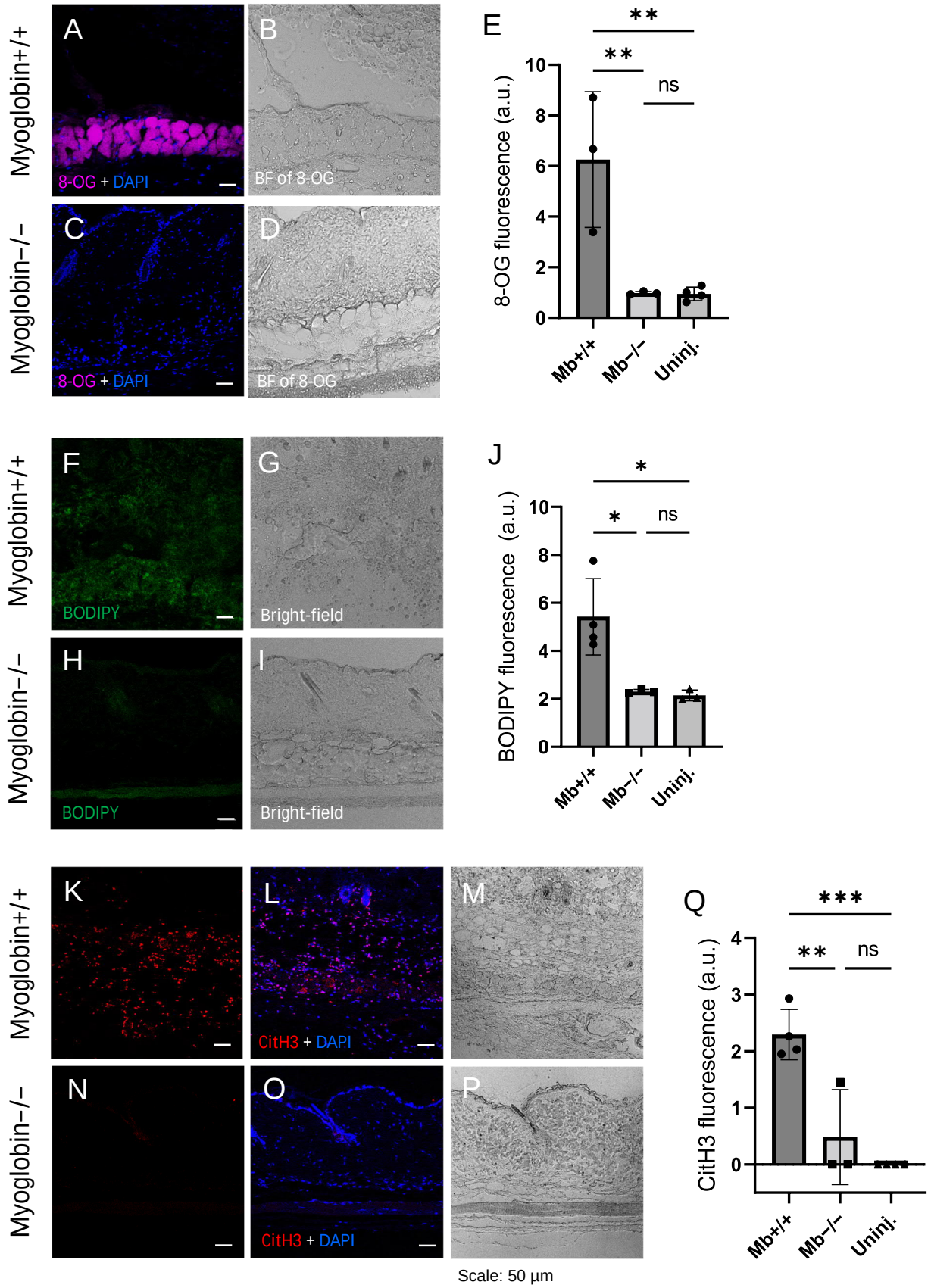

Figure 4: Myoglobin knockout caused a more hospitable wound environment in mPI. (A-D) Immunostaining of 8-oxaguanine (8-OG; in magenta) in Mb+/+ versus Mb−/− mPI. Nuclei were co-stained blue with DAPI. (B) and (D) are bright-field images of (A) and (C), respectively. (E) Quantification of 8-OG staining. (F-I) BODIPY staining (for lipid peroxidation) in Mb+/+ versus Mb−/−. (G) and (I) are bright-field images of (F) and (H), respectively. (J) Quantification of BODIPY staining. (K-P) Immuno-staining for CitH3 (in red) in Mb+/+ versus Mb−/−. (L, O) DNA/nuclei were co-stained blue with DAPI. (M) and (P) are bright-field images of (K) and (N), respectively. Scale bars: 50 µm. (Q) Quantification of CitH3 staining.

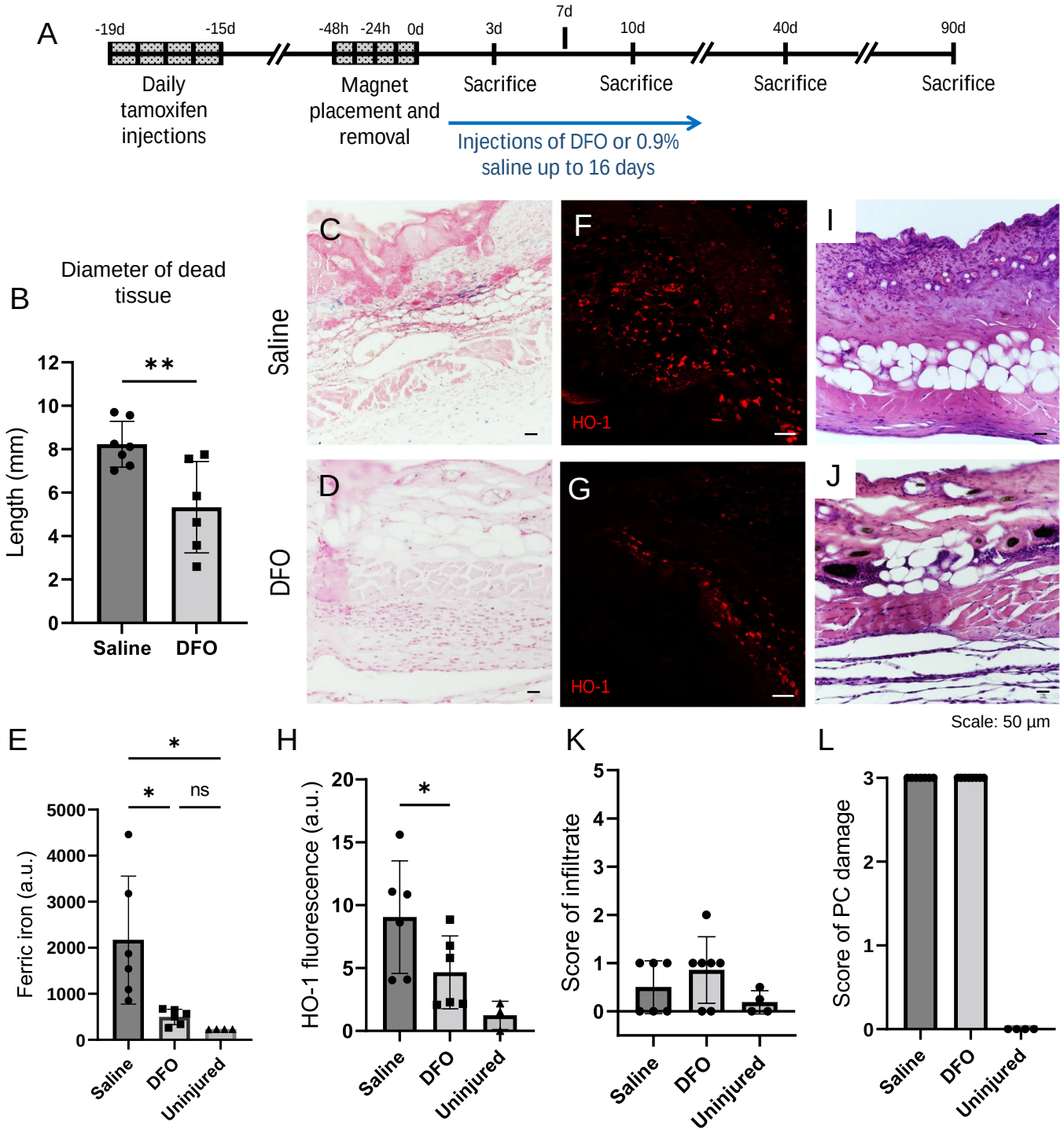

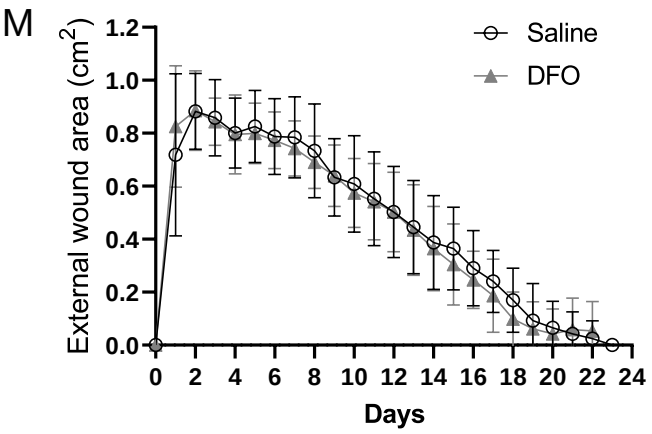

Figure 5: Deferoxamine (DFO) iron chelation therapy decreased iron deposits at day 3 after mPI. (A) Experimental schedule shows confetti fluorescence induction via tamoxifen, mPI induction, treatment with DFO or saline, and tissue harvest. (B) Diameter of the dead region of the panniculus carnosus (PC) muscle in tissue sections from DFO- versus saline-treated mPI, 3 days post-injury. (C-D) Perls' Prussian blue iron staining of (C) saline-treated, and (D) DFO-treated wounds. (E) Quantification of Perls' staining. (F-G) Immunostaining of HO-1 in saline- and DFO-treated. (H) Quantification of HO-1 staining. (I-J) H&E-stained sections of saline- versus DFO-treated mPI at the wound center. (K) Histopathology scoring of immune infiltrate throughout the wound at day 3 between saline- and DFO-treated mPI. (L) Confirmation that injuries were created, according to death of PC tissue at the center of the wound (histopathology scoring where 3 indicates pervasive tissue death). (M) Skin wound area in saline- and DFO-treated mice following mPI.

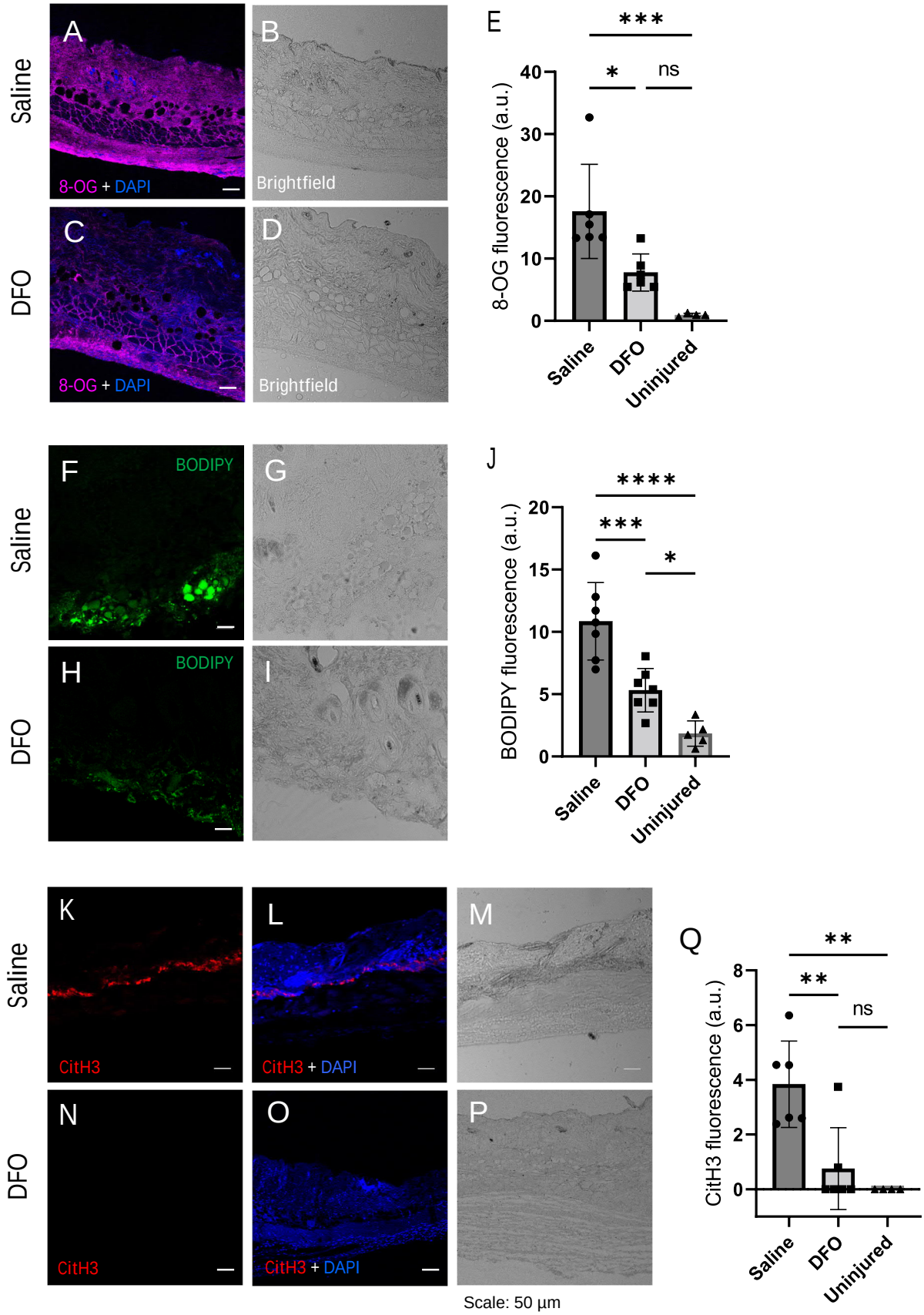

Figure 6: DFO treatment improved the mPI microenvironment (day 3). (A-D) Immunostaining of 8-OG (for DNA damage) in saline-treated versus DFO-treated mPI. Nuclei were stained blue with DAPI. (B) and (D) are bright-field images of (A) and (C), respectively. (E) Quantification of 8-OG. (F-I) BODIPY staining (for lipid peroxidation) and brightfield in saline- versus DFO-treated mPI. (J) Quantification of BODIPY. (K-P) CitH3 immuno-staining with DNA/nuclear co-stain and brightfield in saline- versus DFO-treated mPI. Scale bars: 50 µm. (Q) Quantification of CitH3 staining.

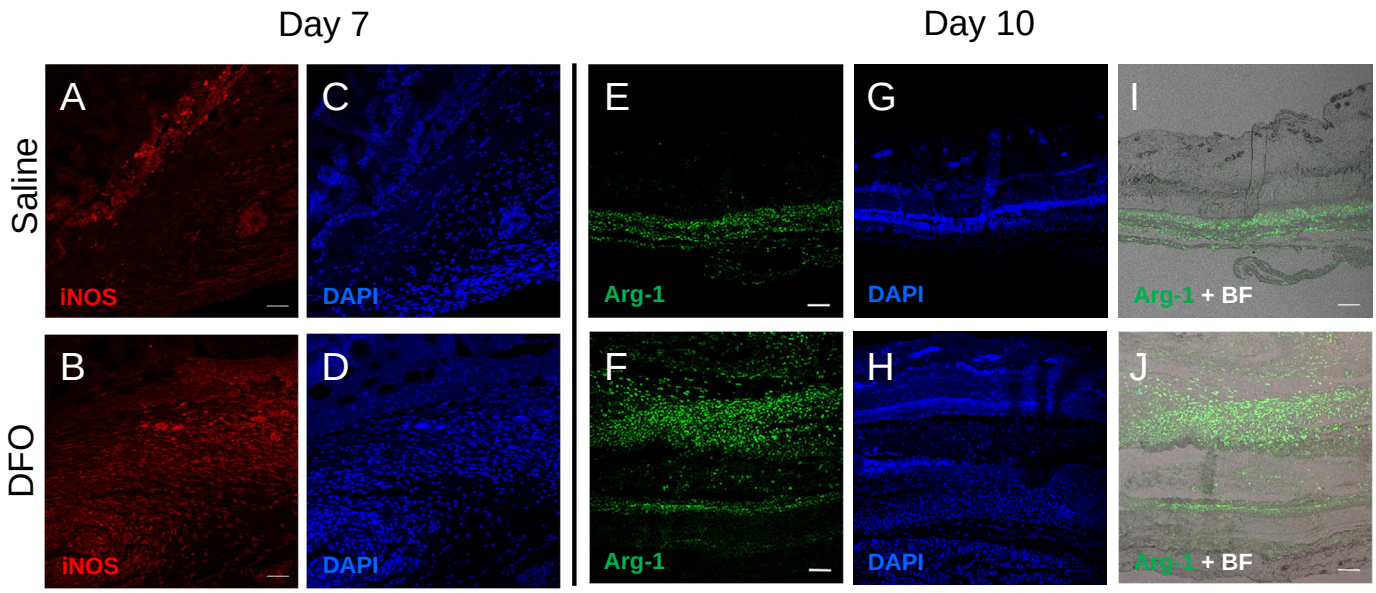

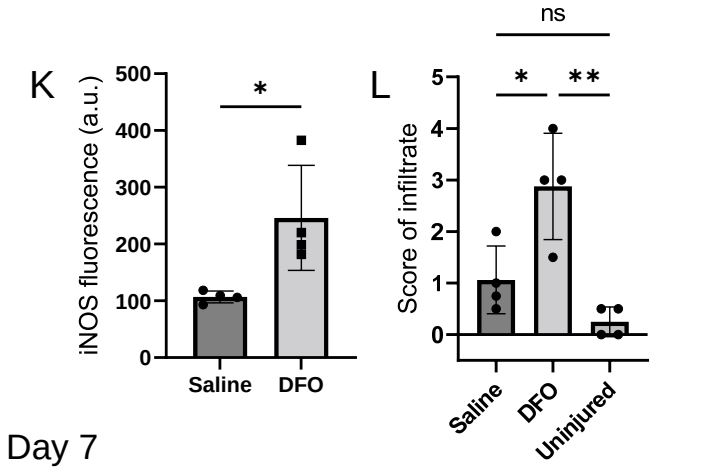

Figure 7: DFO treatment improved immune infiltration (7 and 10 days after mPI). (A-B) Immuno-staining of inducible nitric oxide synthase (iNOS, associated with pro-inflammatory activation) in saline- versus DFO-treated mPI at day 7 post-injury. (C-D) Nuclei are stained blue with DAPI, to show the count of infiltrating cells. (E-F) Immuno-staining of Arginase-1 in saline- versus DFO-treated mPI at day 10 post-injury. (G-H) Nuclei are co-stained blue with DAPI. (I-J) Merged brightfield and Arg-1 immuno-staining. Scale bars: 100 µm. (K) Quantification of iNOS staining at day 7 between saline- and DFO-treated. (L) Scoring of immune infiltrate into the injured tissue at day 7. (M) Scoring of immune infiltrate into the injured tissue at day 10. (N) Quantification of Arg-1 staining. (O) Quantification of DAPI staining. (P) Distance of tissue infiltrated by Arg-1+ cells in saline- versus DFO-treated tissues.

Day 7

Day 10

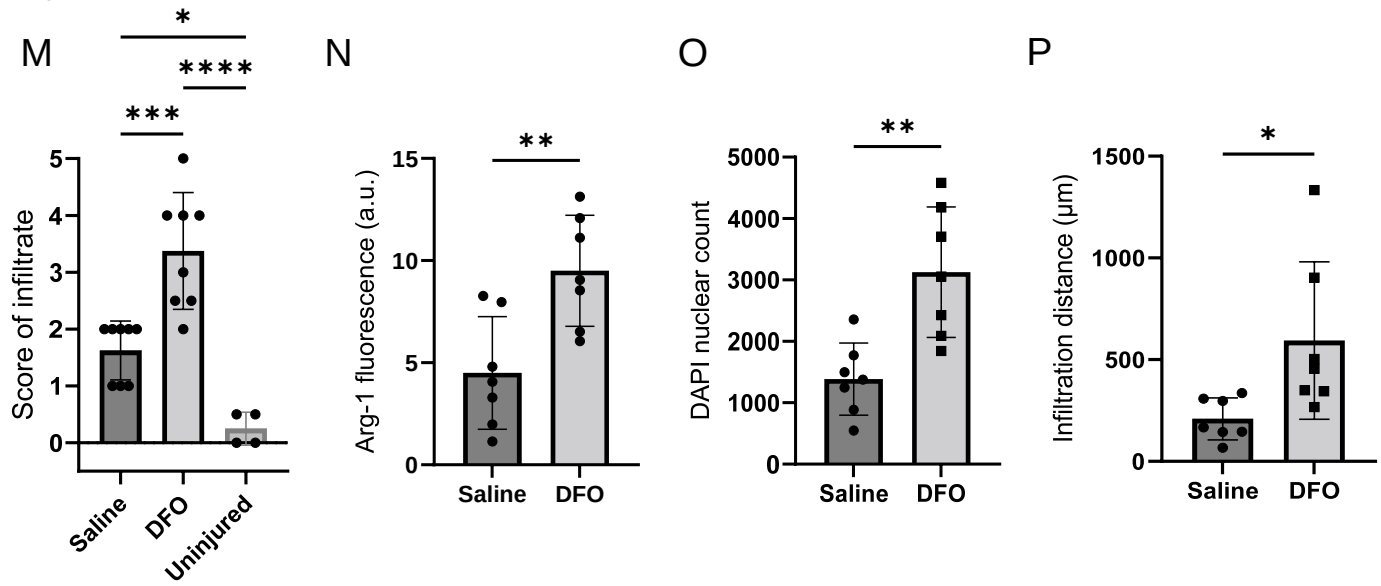

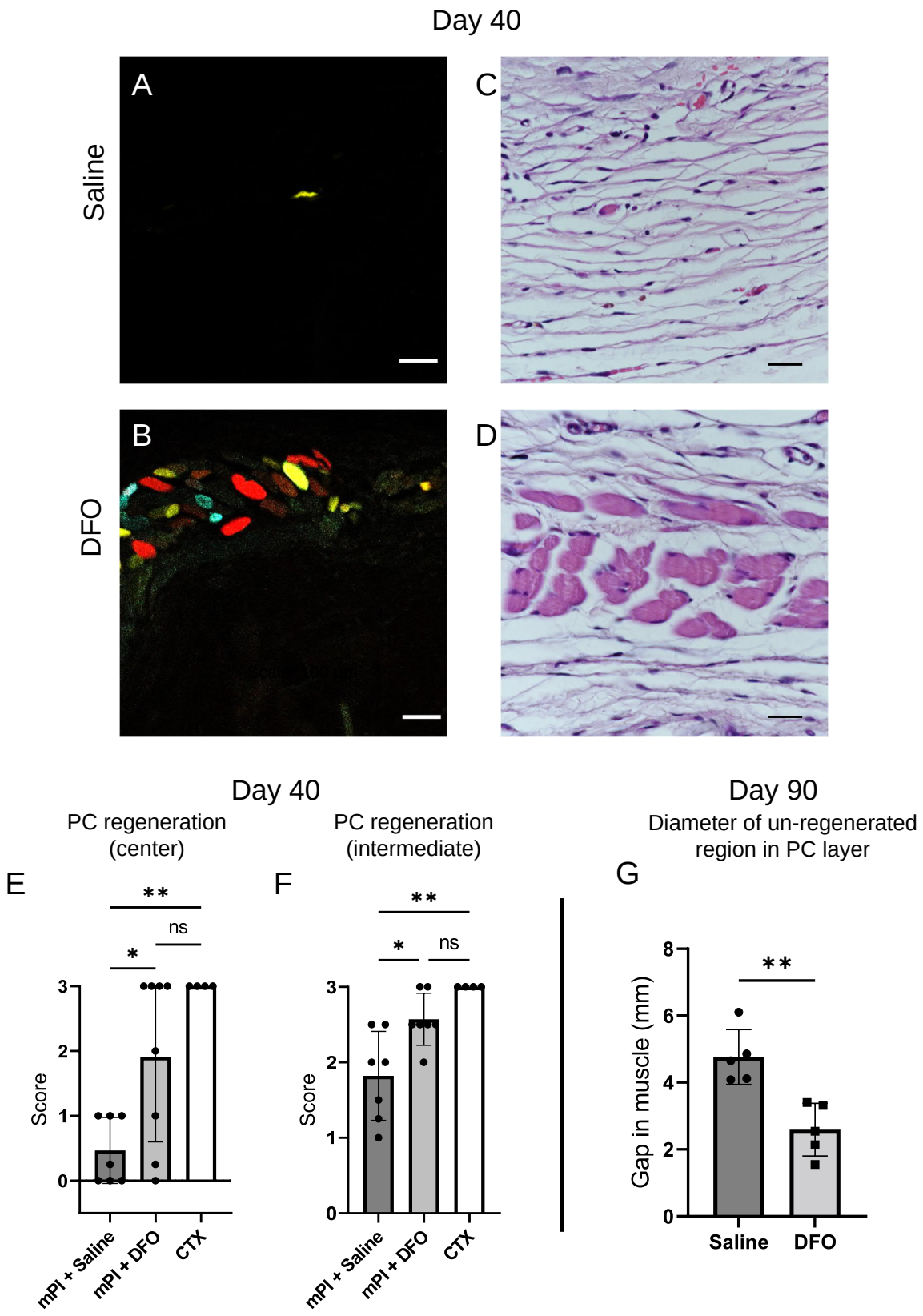

Figure 8: DFO increased the extent of muscle regeneration at day 40 & day 90. (A-B) Confocal fluorescent and (C-D) H&E-stained cross-sections of regenerated muscle fibers from saline- and DFO-treated mPI, 40 days post-injury. Scale bars: 100 µm. (E-F) Histological scoring of PC muscle regeneration in saline- and DFO-treated mPI versus acute CTX-injured tissues at the center and edge of the wound, 40 days post-injury. (G) Diameter of gap (unregenerated region) in PC muscle layer at day 90 post-mPI between saline- and DFO-treated wounds.

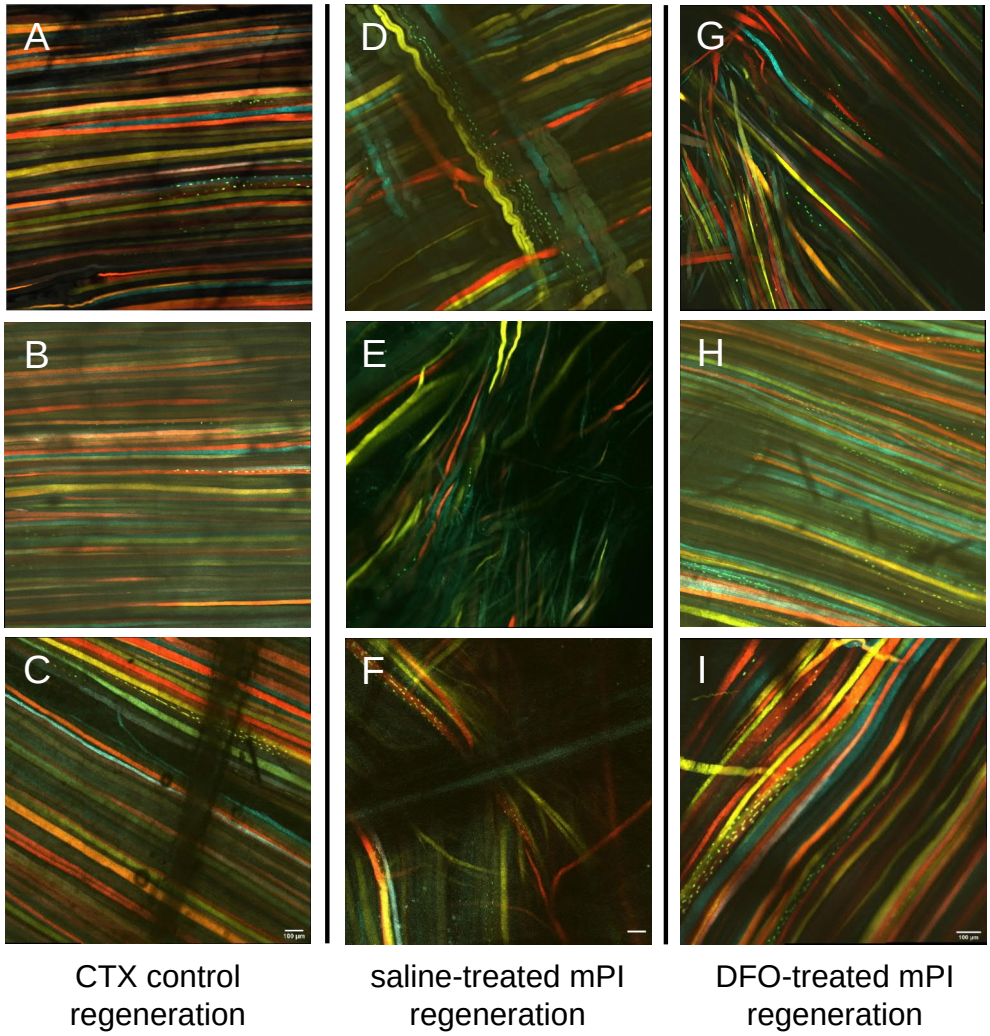

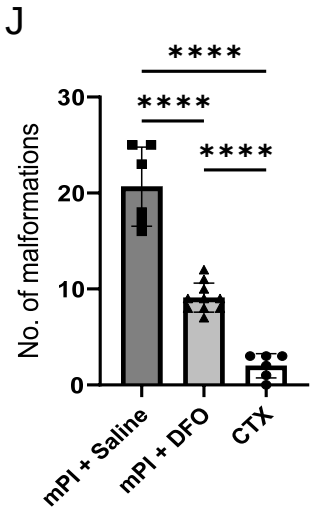

Figure 9: DFO improved muscle morphology. Confocal microscopy of confetti labelled muscle regeneration in ex vivo tissue blocks. Note that unlabelled tissue types such as blood vessels and hair create black shadows on top of the images. (A-C) Left column shows healthy regeneration in the control condition, toxin-induced injury, at 40 days. Experiment was halted at 40 days due to complete regeneration. (D-F) Middle column shows regenerated muscle fibers of saline-treated mPI, 90 days post-injury. Note the presence of non-parallel fibers, bent fibers, and split fibers (i.e., fibers with one or more branches). (G-I) Right column shows regenerated muscle fibers of DFO-treated mPI, 90 days post-injury. Scale bar: 100 μm. (J) Quantification of muscle fiber malformations.